Wake states and frequency selection of a streamwise oscillating cylinder

Justin S. Leontini, David Lo Jacono, Mark C. Thompson

Wake states and frequency selection of a streamwise oscillating cylinder

Justin S. Leontini[1],†, David Lo Jacono[1,2] and Mark C. Thompson[1]

[1]Fluids Laboratory for Aeronautical and Industrial Research (FLAIR), Department of Mechanical and Aerospace Engineering, Monash University, Melbourne, VIC 3800, Australia

[2]Institut de Mécanique des Fluides de Toulouse (IMFT), CNRS, UPS, Université de Toulouse, Allée Camille Soula, F-31400 Toulouse, France

This paper presents the results of an in-depth study of the flow past a streamwise oscillating cylinder, examining the impact of varying the amplitude and frequency of the oscillation, and the Reynolds number of the incoming flow. These findings are presented in a framework that shows that the relationship between the frequency of vortex shedding f_s and the amplitude of oscillation A^* is governed by two primary factors: the first is a reduction of f_s proportional to a series in A^{*2} over a wide range of driving frequencies and Reynolds numbers; the second is nonlinear synchronization when this adjusted f_s is in the vicinity of $N = (1 - f_s/f_d)^{-1}$, where N is an integer. Typically, the influence of higher-order terms is small, and truncation to the first term of the series (A^{*2}) well represents the overall trend of vortex shedding frequency as a function of amplitude. However, discontinuous steps are overlaid on this trend due to the nonlinear synchronization. When f_s is normalized by the Strouhal frequency f_{St} (the frequency of vortex shedding from an unperturbed cylinder), the rate at which f_s/f_{St} decreases with amplitude, at least for $f_d/f_{St} = 1$, shows a linear dependence on the Reynolds number. For a fixed $Re = 175$, the truncated series shows that the rate of decrease of f_s/f_{St} with amplitude varies as $(2 - f_d/f_{St})^{-1/2}$ for $1 \leqslant f_d/f_{St} \leqslant 2$, but is essentially independent of f_d/f_{St} for $f_d/f_{St} < 1$. These trends of the rate of decrease of f_s with respect to amplitude are also used to predict the amplitudes of oscillation around which synchronization occurs. These predicted amplitudes are shown to fall in regions of the parameter space where synchronized modes occur. Further, for the case of varying f_d/f_{St}, a very reasonable prediction of the amplitude of oscillation required for the onset of synchronization to the mode where $f_s = 0.5f_d$ is given. In a similar manner, amplitudes at which $f_s = 0$ are calculated, predicting where the natural vortex shedding is completely supplanted by the forcing. These amplitudes are found to coincide approximately with those at which the onset of a symmetric vortex shedding mode is observed. This result is interpreted as meaning that the symmetric shedding mode occurs when the dynamics crosses over from being dominated by the vortex shedding to being dominated by the forcing.

Key words: flow–structure interactions, vortex shedding, vortex streets

† Email address for correspondence: justin.leontini@monash.edu

1. Introduction

The problem of a circular cylinder in a free stream, performing controlled sinusoidal oscillations in the direction of the flow, presents a range of behaviours of fundamental interest. It bears some relation to flow-induced vibration of cylindrical structures, but also offers a method of active flow control of the classic Kármán vortex street that forms in the wake of a cylinder. The sinusoidal oscillations can also come in the form of adding a periodic perturbation to the inflow, rather than oscillating the cylinder.

The flow response is a function of three parameters: the Reynolds number, $Re = UD/\nu$, where U is the free stream velocity, D is the cylinder diameter, and ν is the kinematic viscosity; the frequency of the oscillatory driving, f_d; and the amplitude of the oscillatory driving, A. The dynamics of the problem is such that the proximity of the driving frequency f_d to the frequency of vortex shedding from an unperturbed cylinder (the Strouhal frequency) f_{St} is a governing parameter, and so the driving frequency is presented as the ratio f_d/f_{St}. The amplitude can be non-dimensionalized by the cylinder diameter D, $A^* = A/D$. Any frequencies can be made non-dimensional by multiplication by D/U, as has been done for the results throughout this paper.

A well-studied phenomenon in this flow is that of synchronization of the vortex shedding to the forcing. Typically, this occurs when the forcing or driving frequency, f_d, is close to twice the frequency of vortex shedding (the Strouhal frequency) from the unperturbed cylinder, f_{St}, or $f_d/f_{St} \simeq 2$. During this synchronization, the vortex shedding frequency from the oscillating cylinder changes to $f_d/2$. Numerous studies, including Tanida, Okajima & Watanabe (1973), Barbi *et al.* (1986), Karniadakis & Triantafyllou (1989), Konstantinidis, Balabani & Yianneskis (2005) and Konstantinidis & Balabani (2007) have investigated cylinders oscillating at these frequencies.

The extent of this synchronization (that is, the amount by which f_d can be detuned from $f_d = 2f_{St}$ where synchronization still occurs) is known to be a function of the amplitude of the forcing. Konstantinidis, Balabani & Yianneskis (2003) show a map of the location of synchronization to the P_2 mode (a mode that is periodic over two oscillation periods), compiled from data from a series of papers in the literature, on the A^*–f_d/f_{St} plane. Interestingly, the plot indicates that there is little dependence on Re, particularly for $Re > 350$, for the location of this boundary, for experiments performed with cylinder oscillations or inflow perturbations. Hall & Griffin (1993) produced a similar map with two-dimensional simulations. Both show that the amplitude required to synchronize to the P_2 mode increases faster than linearly as the driving frequency ratio is reduced from $f_d/f_{St} = 2$.

Synchronization at twice the driving frequency can be understood by considering the unperturbed flow and the symmetry of the driving. The unperturbed, stationary cylinder generates a wake consisting of the Kármán vortex street, an essentially two-dimensional flow consisting of two staggered rows of vortices. This wake possesses a spatio-temporal symmetry, i.e. evolution forward in time by half a period plus reflection in space about the wake centreline gives the same flow. In terms of the streamwise component of the velocity field u, $u(x, y, t) = u(x, -y, t + T_{St}/2)$, where $T_{St} = 1/f_{St}$ is the period of vortex shedding. The forcing, on the other hand, does not possess this spatio-temporal symmetry. It possesses a spatial symmetry, $u(x, y, t) = u(x, -y, t)$, and a temporal symmetry (or periodicity), $u(x, y, t) = u(x, y, t + T)$. Typically, then, adding this forcing to the Kármán vortex street breaks a symmetry of the flow, and the forcing must therefore remove the spatio-temporal symmetry of the flow. However, when the forcing frequency is such that $f_d/f_{St} = 2$, $T = T_{St}/2$. Then, on the time scale of the unperturbed cylinder vortex shedding T_{St}, the forcing does

have the same spatio-temporal symmetry, and no symmetry is broken by the forcing, allowing the flow to neatly synchronize with the driving.

As a side note, this same argument explains why *transverse* forcing, where the cylinder is oscillated across the stream, synchronizes when $f_d \simeq f_{St}$ (Williamson & Roshko 1988; Meneghini & Bearman 1995; Leontini *et al.* 2006). The transverse forcing shares the spatio-temporal symmetry of the unperturbed flow, and hence does not induce a symmetry breaking at vanishing amplitudes.

An important point to note is that, for this synchronization to occur, the forcing must possess the spatio-temporal symmetry *on the same time scale* as the wake. If there is a mechanism by which this time scale can be changed, the frequency of the forcing at which synchronization will occur will vary from exactly $f_d/f_{St} = 2$. As noted in the study of Konstantinidis *et al.* (2003) (among others), if the amplitude A^* of the forcing is increased, synchronization can occur at forcing frequencies where f_d/f_{St} is further from 2. This can be interpreted as the amplitude of oscillation having some control on the time scale of the flow.

Mureithi & Rodriguez (2005) and Rodriguez & Mureithi (2006) noted a decrease in the primary wake frequency when the flow is not synchronized to the driving, with increasing amplitude for $f_d/f_{St} = 1$. This work, along with that of Mureithi *et al.* (2010), gives a low-order model derived directly from the symmetries of the Kármán shedding and the forcing to try to identify the series of bifurcations in the wake. The low-order model predicted that, when the amplitude of forcing is small, the flow will be quasi-periodic, a direct consequence of the interaction of two frequencies: that of the driving, and the new vortex shedding frequency (or new time scale) dictated by the amplitude of the forcing. At higher amplitudes, the model predicted that the vortex shedding frequency would synchronize to half of the driving frequency. This work clearly shows the impact of the symmetry of the forcing, a point also observed by Ongoren & Rockwell (1988).

The prediction of quasi-periodicity in the flow when it is not synchronized to the driving is consistent with observations, both experimental and numerical. The experimental results of Cetiner & Rockwell (2001) show this over a wide range of oscillation frequencies, $0.37 \leqslant f_d/f_{St} \leqslant 2.27$, as well as a wide range of vortex shedding modes. Kim & Williams (2006) explicitly showed the presence of the new vortex shedding frequency, and showed that the frequency spectra contained components that consisted of sums and differences of this new frequency and the driving frequency. Numerically, Al-Mdallal, Lawrence & Kocabiyik (2007), Marzouk & Nayfeh (2009) and Perdikaris, Kaitsis & Triantafyllou (2009) saw quasi-periodicity when the amplitude of the forcing was below that required for synchronization. Marzouk & Nayfeh (2009) also observed that the flow could synchronize to the forcing over multiple oscillation cycles (more than the two periods of the P_2 mode), confirming the experimental observations of Yokoi & Kamemoto (1994).

One explanation for the presence of two frequencies is the concept of an intrinsic vortex formation time associated with the flow, which governs the rate at which vortices are formed and shed into the wake. Promising work in this direction has been performed by Jeon & Gharib (2004).

Xu, Zhou & Wang (2006) present an argument in terms of vorticity production at the surface of the cylinder to explain the onset of the symmetric shedding mode. They decomposed the vorticity production into two components: that associated with the oscillation of a cylinder in quiescent fluid, and that associated with the flow past a stationary cylinder. This argument led them to conclude that the critical A^* at which the symmetric shedding mode could be expected scaled with $1/(f_d/f_{St})$. This is similar

to the predictions of this paper, which find the critical A^* decreases with increasing f_d/f_{St}, if different in form.

Konstantinidis, Balabani & Yianneskis (2007) showed that, even when locked to the P_2 mode, the exact wake configuration can apparently switch (in their case between a $2S$ and $2P$ mode).

On a related problem of inline forcing, but with non-sinusoidal waveforms, Konstantinidis & Bouris (2009) showed that a number of wake configurations were possible for the same primary frequency and amplitude. This shows that, away from the cylinder, where the exact shape of the body or time history of the forcing is not important, there are a number of apparently stable vortex configurations that can exist with the same spatio-temporal symmetries.

Jauvtis & Williamson (2005), for a cylinder free to vibrate in both the cross-flow and inline directions, showed a symmetric mode that consisted of inline oscillation only. A second mode with symmetry similar to the Kármán vortex street was also found, but this consisted of the cylinder tracing a figure-of-eight path. It should be noted that, for this figure-of-eight path to maintain the spatio-temporal symmetry of the Kármán vortex street, the inline component needs to oscillate at twice the frequency of the cross-flow component, or, equivalently, at twice the frequency of the vortex shedding.

This paper attempts to explain how many of these apparently disparate phenomena arise from two root causes, across a wide range of Reynolds numbers Re and driving frequencies f_d. The first cause is that the oscillating body acts as a wavemaker, the frequency of the waves created being a function of the oscillation amplitude A^*. These generated waves are represented by the shedding of vortices in the wake at a frequency f_s. This vortex shedding interacts with the acceleration from the oscillatory driving, leading to frequency and amplitude modulation. The product is a quasi-periodic oscillation of the wake, which produces a complicated spectrum, the contents of which have been explained in Leontini, Lo Jacono & Thompson (2011). On top of this vortex shedding at a frequency f_s, the second cause is nonlinear synchronization. This paper shows that synchronization occurs when the aforementioned f_s is in the vicinity where $N = (1 - f_s/f_d)^{-1}$, N being an integer and f_d being the driving frequency.

It is proposed that, initially ignoring the nonlinear synchronization, the vortex shedding frequency can be represented by a series of the form

$$f_s(Re, f_d, A^*) = f_{St} + \Gamma_1(Re, f_d)A^{*2} + \Gamma_2(Re, f_d)A^{*4} + \cdots. \tag{1.1}$$

In fact, it is shown that, for a wide range of Re and f_d, a very good representation of the vortex shedding frequency (still ignoring nonlinear synchronization) is given by truncating this series at the first term, namely

$$f_s(Re, f_d, A^*) = f_{St} + \Gamma_1(Re, f_d)A^{*2}, \tag{1.2}$$

extending the findings of Leontini *et al.* (2011) at a single value of Re and f_d. It should be noted that Γ_1 is expected to be negative, as increased amplitudes of oscillation result in lower frequencies of vortex shedding.

The impact on (1.2) of the nonlinear synchronization when f_s is in the vicinity of $N = (1 - f_s/f_d)^{-1}$ is to introduce a series of discontinuous 'steps', as the synchronization forces the vortex shedding to move to a frequency in step with the driving. The amplitude range of each of these steps, one step for each integer value of N, brackets the amplitude at which (1.2) 'predicts' a value of f_s that results in the given integer value of N. For low values of N, typically $N \leqslant 4$, these synchronization regions appear to overlap, resulting in bistability and hysteretic transitions.

Simply considering these two causes, i.e. the vortex shedding frequency lowering with A^{*2}, and nonlinear synchronization, the appearance of a very wide variety of flow states, ranging from quasi-periodicity, long-period synchronized states, chaos and symmetric shedding, can be shown to arise from the same underlying dynamics. Equation (1.2) shows that the appearance of these states, including synchronization to the P_2 mode, often referred to as 'lock-in' or 'lock-on', is governed by the rate of decrease of f_s with A^* or Γ_1.

Section 2 presents an outline of the simulation methodology and the methodology used for data fitting. Section 3.1 presents measures of global scalars, such as lift and drag, and data from example cases to illustrate how the different regimes have been identified. Section 3.2 presents results where the ratio of the driving frequency to the fixed cylinder vortex shedding frequency $f_d/f_{St} = 1$, and $75 \leqslant Re \leqslant 250$. Section 3.3 then presents results for $1 \leqslant f_d/f_{St} \leqslant 2$, for a fixed $Re = 175$. Some concluding remarks are then given in § 4.

2. Methodology

2.1. *Simulation scheme*

Two-dimensional direct numerical simulations of the flow past a streamwise oscillating cylinder have been conducted. The code used is a spectral element code solving the incompressible Navier–Stokes equations. Lagrange polynomials (eighth order for the simulations of this paper) are used as the shape functions over each quadrilateral element. These quadrilateral elements can have straight or constant-radius curved sides, so that the surface of the cylinder can be represented exactly. The equations are solved in an accelerating frame of reference, attached to the moving cylinder. This results in an extra term, accounting for the acceleration of the frame (which is prescribed by the controlled motion of the cylinder) being added to the Navier–Stokes equations. This removes the need for any mesh deformation, and removes the ambiguity of varying mesh resolution throughout the simulation.

A three-way time-splitting method is employed for the temporal integration, which results in an equation each for the advection and frame acceleration, pressure and diffusion terms of the Navier–Stokes equations. The advection equation is solved explicitly using a second-order Adams–Bashforth scheme. By taking the divergence of the pressure equation and invoking the continuity constraint, a Poisson equation is formed that can be solved for the pressure, so that this pressure can then be used to finalize the integration of the original pressure equation. Finally, the diffusion equation is solved using a second-order implicit Crank–Nicolson scheme with theta correction.

A domain extending $15D$ upstream and to either side and $53D$ downstream of the cylinder centre was employed. This domain was divided into 1696 quadrilateral elements, with the majority focused in the boundary layer and wake regions of the flow. Dirichlet boundary conditions $u = U - u_{cyl}$, where u_{cyl} is the prescribed cylinder velocity, are employed at the upstream and transverse boundaries, and a no-slip condition employed at the cylinder surface. At the downstream boundary, an outflow Neumann condition $\partial \boldsymbol{u}/\partial \boldsymbol{n}$, where $\boldsymbol{u}$ is the velocity vector and $\boldsymbol{n}$ is the normal vector, has been employed. For the pressure, a Neumann condition, where the normal gradient is calculated directly from the Navier–Stokes equations, has been used at all Dirichlet boundaries (Gresho & Sani 1987), and a Dirichlet condition of $p = 0$, where p is the pressure, has been used at the downstream outflow boundary.

This code is well validated for use in bluff-body flows, having been used for three-dimensional cylinder simulations (Thompson, Hourigan & Sheridan 1996), transverse

oscillation simulations (Leontini *et al.* 2006; Leontini, Thompson & Hourigan 2007), rotational oscillation simulations (Lo Jacono *et al.* 2010), combined rotational and transverse oscillation simulations (Nazarinia *et al.* 2009) and also for previous streamwise oscillation studies using the same mesh (Leontini *et al.* 2011). Further details of the method can be found in Thompson *et al.* (1996, 2006), and an in-depth treatment of the spectral element method in general can be found in Karniadakis & Sherwin (2005).

Two-dimensional simulations have been conducted even though the highest Reynolds numbers used ($Re = 250$ for $f_d/f_{St} = 1$) exceed the value of $Re = 190$ at which three-dimensional transition is known to occur for the case of flow past a fixed cylinder (Williamson 1988; Barkley & Henderson 1996). This may mean that some of the flow states observed during this study are not accessible in reality. However, the focus here is on the general dynamics of frequency selection, and the identification of the basic states obtained. It therefore seems appropriate to conduct an in-depth two-dimensional study prior to attempting to deal with the complexity introduced by full three-dimensional flow. Indeed, understanding the underlying two-dimensional states is a prerequisite to attempting to understand the series of bifurcations that lead to the fully developed three-dimensional flow.

2.2. *Identification of points suitable for data fitting*

A major focus of this paper is the quantification of the change in vortex shedding frequency as a function of the cylinder oscillation. To do this, the frequency content of the lift force signal (the force in the cross-stream direction) has been found, and the primary frequency identified as the vortex shedding frequency, f_s. Generally, the lift force signal is quasi-periodic, owing to interaction between the driving frequency f_d and f_s. However, the physics are quite intricate, and there are a number of resonances and nonlinear synchronizations that can occur between f_d and f_s. These resonances move f_s from its 'natural' value (the value it would obtain without the synchronization) to some other nearby value.

Therefore, only the data from simulations where the flow was deemed to be quasi-periodic have been used when data fitting to ascertain the variation of f_s as a function of the oscillation. As the results show, this approach leads to a very good estimate of the basic vortex shedding frequency trends, which can then be used to predict the onset of synchronization and resonance, as well as other behaviours.

Figure 1 shows an example of f_s as a function of A^* for $Re = 175$, $f_d/f_{St} = 1$. In the figure, quasi-periodic points are marked with closed symbols, and the points deemed synchronized are marked with open symbols. A line of best fit of the form of (1.2) has been added, fitted to the quasi-periodic points only. The figure clearly shows that this process results in a line of best fit that well represents the true trend of f_s.

3. Results

3.1. *Global scalars and example cases*

The major focus of this paper is on the frequency selection properties of the streamwise oscillating cylinder wake as a function of the amplitude and frequency of oscillation, and the Reynolds number. However, this section presents results of the measurements of global scalars, such as the mean drag force, and a number of example cases. These example cases have been selected to span a range of all the input parameters, to provide evidence that the findings of this paper apply across all the parameters tested, and are not restricted to a few special cases.

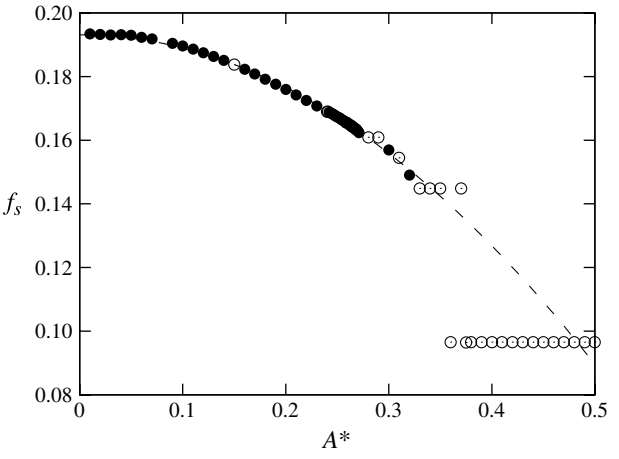

FIGURE 1. The frequency of vortex shedding, f_s, as a function of A^*, for $Re = 175$, $f_d/f_{St} = 1$. Points deemed quasi-periodic are marked with closed circles (●); points deemed synchronized are marked with open circles (○). The solid line marks a fit of the form of (1.2) to the quasi-periodic points only. It is clear that this fit well represents the overall trend of the vortex shedding frequency.

Figure 2 presents the mean drag coefficient $\overline{C_D}$ and the standard deviation of the lift coefficient, or the root-mean-square value (r.m.s.) after the removal of the mean $C_{L(rms)}$, as a function of amplitude A^* for six values of f_d/f_{St} at $Re = 175$. All the plots share the same scale on the abscissa, while the ordinate axes are varied to make the plots easier to read. The different symbols on the plots mark qualitatively different flow states, and the same symbols are used throughout the paper to represent the same flow state. Also marked on the plots of $\overline{C_D}$ with a vertical line is the value of A^* at which a P_2 mode was observed.

The generic response type for small-amplitude oscillations is a quasi-periodic flow. As the amplitude is increased, a series of synchronizations become possible, and the flow becomes periodic over an integer multiple N of the driving period. These periodic responses have been labelled as P_N. This integer N reduces as the amplitude is increased. Figure 2 shows that, for $N > 4$, which occurs at amplitudes smaller than that at which synchronization to the P_2 mode occurs, synchronization to a P_N mode has little impact on the forces. For small amplitudes, the $\overline{C_D}$ and $C_{L(rms)}$ typically increase approximately linearly with A^*, regardless of f_d/f_{St}.

However, at least for the case of $f_d/f_{St} = 1$, synchronization to the P_4 mode results in a distinct change in the trend of the forces, with the plots of both $\overline{C_D}$ and $C_{L(rms)}$ showing a distinct change in gradient. For $f_d/f_{St} > 1$, the change in gradient is only noticed with synchronization to the P_2 mode. This is most likely due to the P_4 mode becoming more difficult to resolve, as the transition between the modes appears to be hysteretic, and the P_4 mode is overwhelmed by the more dominant P_2 mode. Regardless of whether the change in gradient corresponds to synchronization to the P_4 or P_2 mode, further increases in A^* see both $\overline{C_D}$ and $C_{L(rms)}$ continue to increase approximately linearly.

The results for $f_d/f_{St} = 0.8$ show a different trend. At small amplitudes, the behaviour is the same as at higher values of f_d/f_{St}; the quasi-periodic response sees $\overline{C_D}$ and $C_{L(rms)}$ increase approximately linearly with A^*. However, the flow

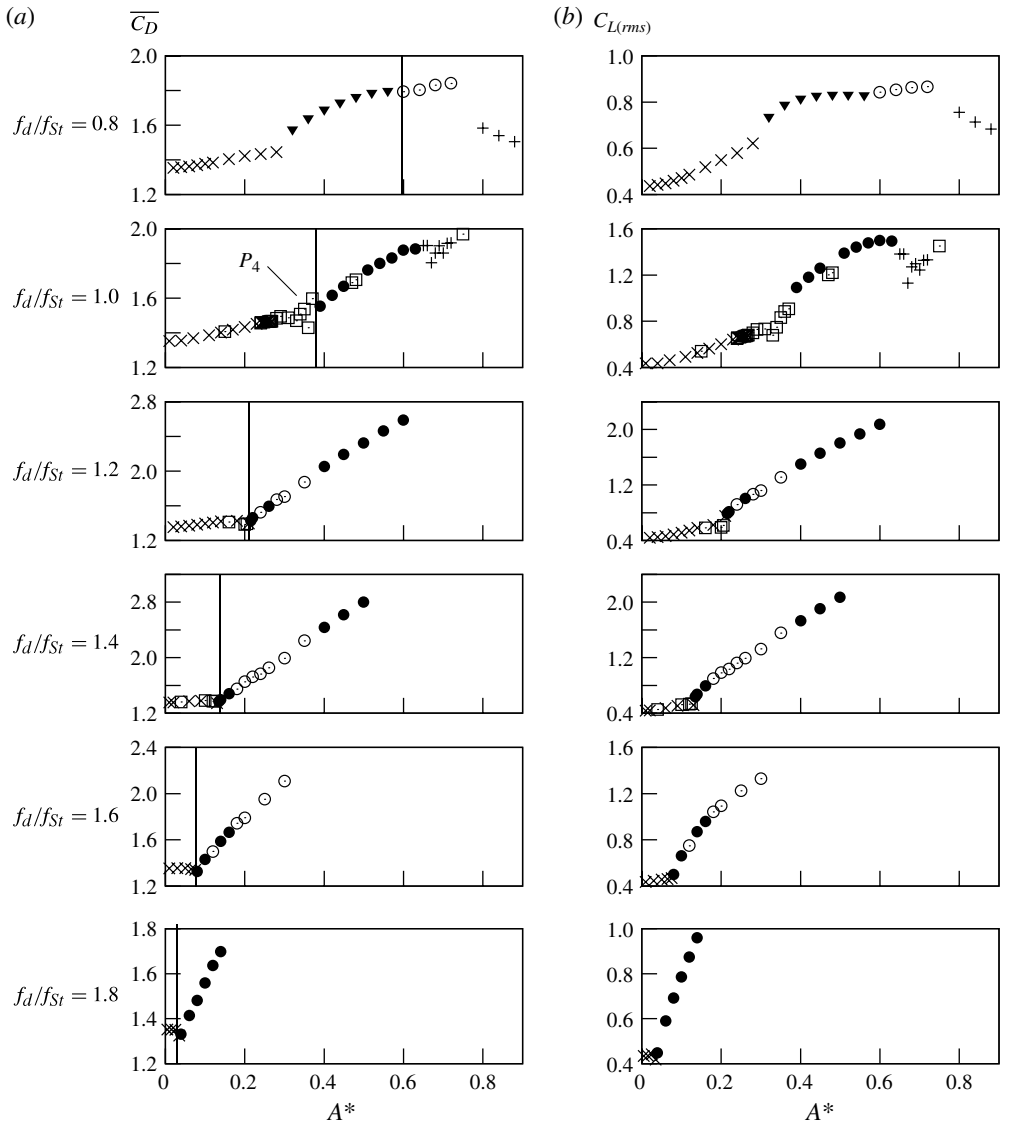

FIGURE 2. (*a*) Mean drag coefficient $\overline{C_D}$ and (*b*) r.m.s. lift coefficient $C_{L(rms)}$ for $Re = 175$, and various values of f_d/f_{St}, increasing from top to bottom. Symbols depict different response regimes delineated by their spatial and temporal symmetries: P_1 (▼); P_2 (●); P_2, non-zero mean lift (○); chaos (+); P_N other than P_1 or P_2 (□); quasi-periodicity (×). Vertical lines on the $\overline{C_D}$ panels mark the onset of the P_2 modes. Both scalars show a distinct change in trend when synchronization to any of the P_1 or P_2 modes occurs for all f_d/f_{St}, and they also show a distinct change with synchronization to the P_4 mode for $f_d/f_{St} = 1$. Synchronization to other P_N modes interleaved with regions of quasi-periodicity has little impact on the forces, except for the locking to a P_4 mode when $f_d/f_{St} = 1$.

synchronizes to a P_1 mode at around $A^* = 0.30$, where a jump in the value of both $\overline{C_D}$ and $C_{L(rms)}$ is observed as well as a change in gradient (the apparent jump in value may simply be due to a very rapidly changing value that the resolution of A^* used is not adequate to resolve). Further increases in A^* beyond this jump see

both force coefficients flatten off, before synchronization to the P_2 mode. The loss of synchronization at high amplitudes, shown for $f_d/f_{St} = 0.8$ and $f_d/f_{St} = 1$, results in a chaotic flow and a reduction in $\overline{C_D}$ and $C_{L(rms)}$, which is particularly clear for $f_d/f_{St} = 0.8$.

The synchronization to a P_1 mode can only occur for values of $f_d/f_{St} < 1$. It is due to the primary frequency of vortex shedding, f_s, matching the driving frequency, f_d. The impact of the oscillation amplitude on f_s regardless of f_d/f_{St} is to lower it, so, for an amplitude where $f_s \simeq f_d$ to exist, f_s at $A^* = 0$ must be above f_d. By definition, this only occurs when $f_d/f_{St} = 1$. This point is discussed further in § 3.3.

Figure 2 presents force coefficients resulting from a number of qualitatively different flows. The same process as was used in Leontini *et al.* (2011) for cases of $Re = 175$, $f_d/f_{St} = 1$ was used for qualifying each response type. Regardless, examples of the evidence used for the identification of these different flow regimes when $Re = 150$ and $f_d/f_{St} = 1$ are presented in figures 3 and 4. Figures 5 and 6 present this evidence for the case of $Re = 175$, $f_d/f_{St} = 1.4$.

Figure 3 presents snapshots of the wake visualized using vorticity and Lissajous plots of the lift versus drag coefficient for amplitudes $A^* = 0.35$, 0.40, 0.45 and 0.90, for $Re = 150$, $f_d/f_{St} = 1$. The lift and drag coefficients have been sampled once per oscillation period, and the values plotted as points on the Lissajous plots, to produce a type of Poincaré section. These cases represent a quasi-periodic response, a P_4 mode, a P_2 mode and a symmetric shedding mode.

The qualitative difference between the P_4, P_2 and symmetric modes' wake structure is clear, especially when the vortices shed over N cycles are highlighted, as they are in figure 3 by the boxes on the wake images. The difference between the quasi-periodic mode and the P_4 mode are not as distinct, and more robust measures are required to fully delineate these regimes. This is even more pertinent for P_N modes of higher N.

The Poincaré sections are very effective in this regard, as they show the synchronization very clearly, with the number of distinct points in the section equal to N. The quasi-periodicity of the case at $A^* = 0.35$ is also well represented by the Poincaré section, with the points drawing out a smooth curve. It should be noted that a chaotic response would not draw such a smooth curve, but rather would result in scattered points.

Further quantitative evidence of the difference between the regimes can be found via inspection of the time history of the lift coefficient and the resulting frequency spectra. Figure 4 presents these for the same cases as the wake images and Poincaré sections of figure 3. The spectra were produced by discarding the initial transient section of the time history, removing the mean and applying a Hanning window to the remaining section, and then taking the discrete Fourier transform. The time history of the quasi-periodic case at $A^* = 0.35$ is clearly modulated. The associated frequency spectrum is complex, but not purely broadband, with distinct spikes at regularly spaced intervals. This regular spacing comes from the fact that the quasi-periodic flow is characterized by regular vortex shedding at f_s, which is then frequency and amplitude modulated, as explained in detail in Leontini *et al.* (2011).

There is a clear difference between the spectrum produced by the quasi-periodic flow and the P_4 mode, and then the P_2 mode, as A^* is increased. The loss of modulation with the onset of the P_N modes is also clear in the time histories.

The onset of the symmetric mode is also very clear, with the lift coefficient remaining very close to zero ($C_L < 10^{-5}$) over the entire time history of the simulation. Because of this, the spectrum presented for $A^* = 0.900$ in figure 4 is that of the drag

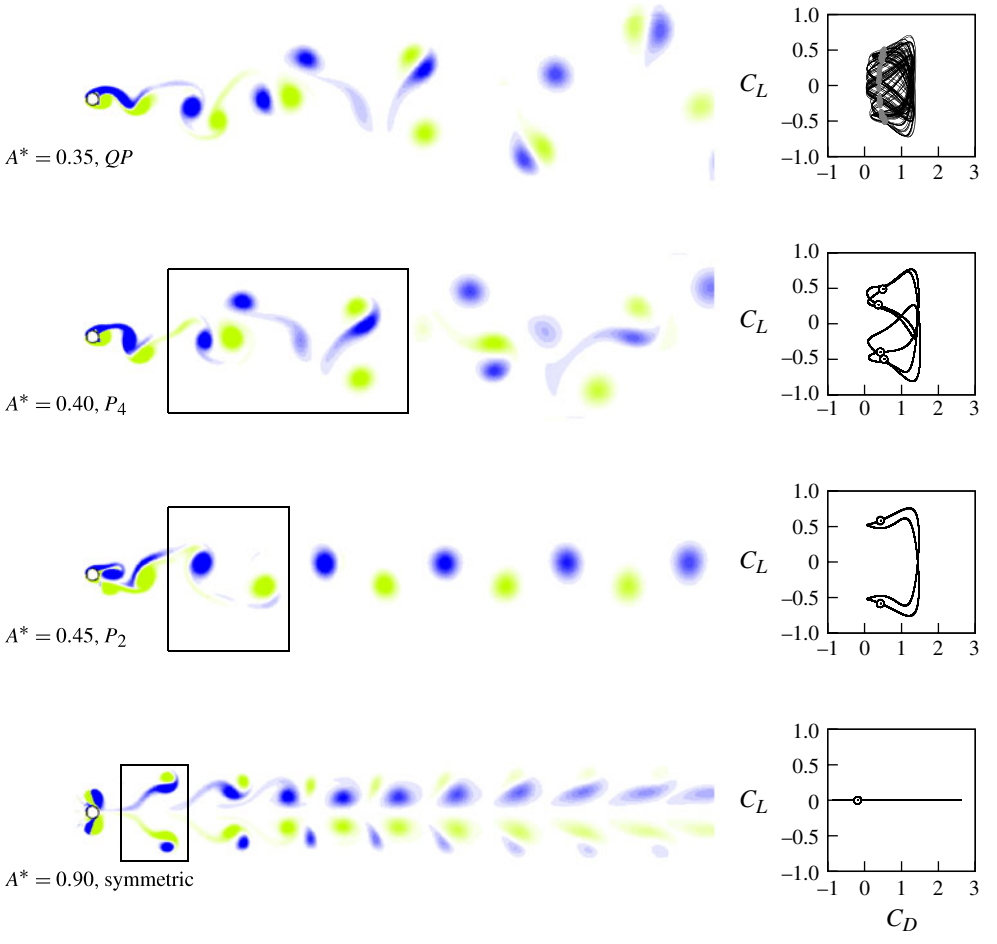

FIGURE 3. (Colour online) Snapshots of vorticity at levels ± 1, and Lissajous plots of lift coefficient C_L against drag coefficient C_D, for $Re = 150$, $f_d/f_{St} = 1$, for a series of oscillation amplitudes, increasing from top to bottom. The boxes on the wake images mark the vortices shed over one repetition, or N cylinder oscillations. The points on the Lissajous plots come from sampling the lift and drag once each oscillation period. The data presented are the same as those of figure 4.

coefficient, which clearly shows that the symmetric mode oscillates at the frequency of the forcing.

The same qualitative features define the flow regimes identified regardless of the Reynolds number and driving frequency. Figure 5 presents wakes and Lissajous plots, overlaid with Poincaré sections when $Re = 175$, $f_d/f_{St} = 1.4$. The cases presented are for amplitudes of oscillation $A^* = 0.06$, 0.10, 0.14 and 0.18. These cases correspond to a quasi-periodic mode, a P_3 mode, a P_2 mode and a P_2 mode with a non-zero mean lift, respectively.

Again, the wake configurations clearly show the difference between all the synchronized modes. Interestingly, the P_2 mode with a non-zero mean lift is shown to have a very similar vortex formation process, and therefore near-wake configuration,

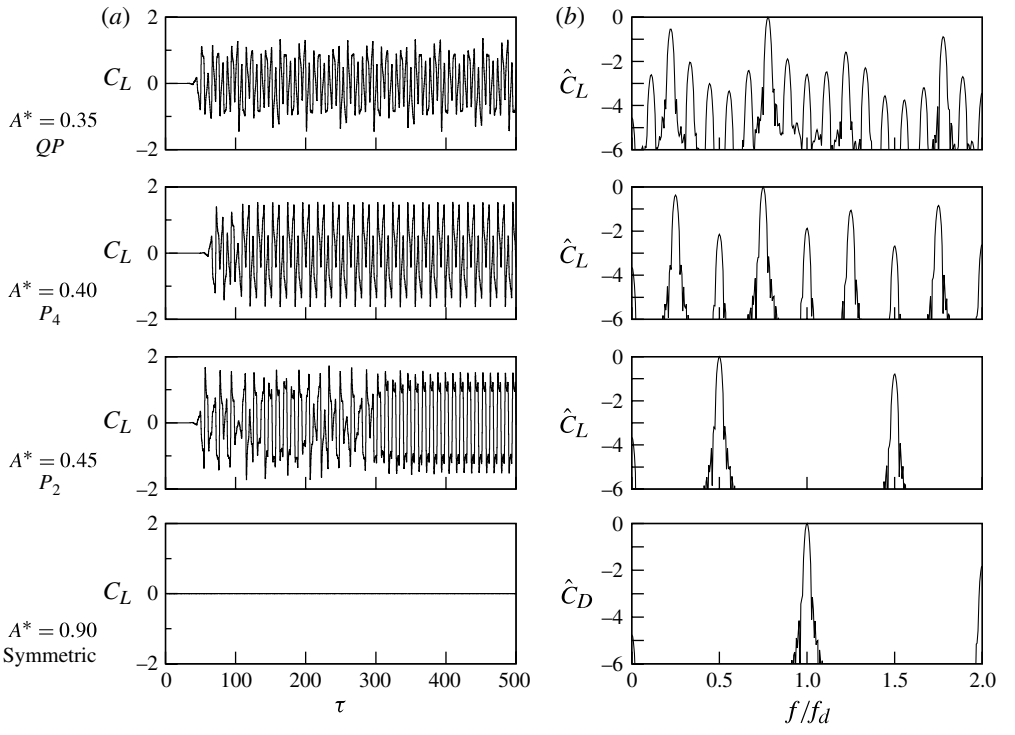

FIGURE 4. (*a*) Time histories of the lift coefficient C_L and (*b*) portions of the frequency spectra presented on a log scale obtained from taking the Fourier transform of the lift coefficient history; $Re = 150$, $f_d/f_{St} = 1$. For the symmetric case at $A^* = 0.900$, the spectrum of the drag coefficient C_D is shown, as the lift coefficient does not oscillate. The amplitude of oscillation increases from top to bottom. The change in signature of the time history and spectrum as the flow moves from quasi-periodic to the various synchronized modes is clear. The data presented are the same as those of figure 3.

as the regular P_2 mode, but the strengths of the positive and negative vortices are not equal, resulting in pairs of vortices self-propelling away from the wake centreline further downstream. The Poincaré sections unequivocally distinguish between the quasi-periodic and synchronized modes.

Figure 6 presents the time histories and frequency spectra for the same cases as presented in figure 5. Some amplitude modulation of the time history is evident for the quasi-periodic case at $A^* = 0.06$, but inspection of the frequency spectra shows very clear evidence of both amplitude and frequency modulation. Again, there is a clear distinction between the character of the frequency spectra of the quasi-periodic and synchronized cases.

3.2. *Dependence on Re when f_d/f_{St} is fixed*

The results of this section report on simulations where the driving frequency $f_d = f_{St}$, but Re has been varied from $Re = 75$ to $Re = 250$. For each value of Re, simulations of flow past a stationary cylinder were first conducted to ascertain the value of f_{St}, and the subsequent oscillating cylinder simulations used this value as the driving frequency f_d. All the simulations were started from rest, and run up to $\tau = 1000$, where $\tau = tU/D$, and t is time. For $Re = 75$, this represents approximately 152

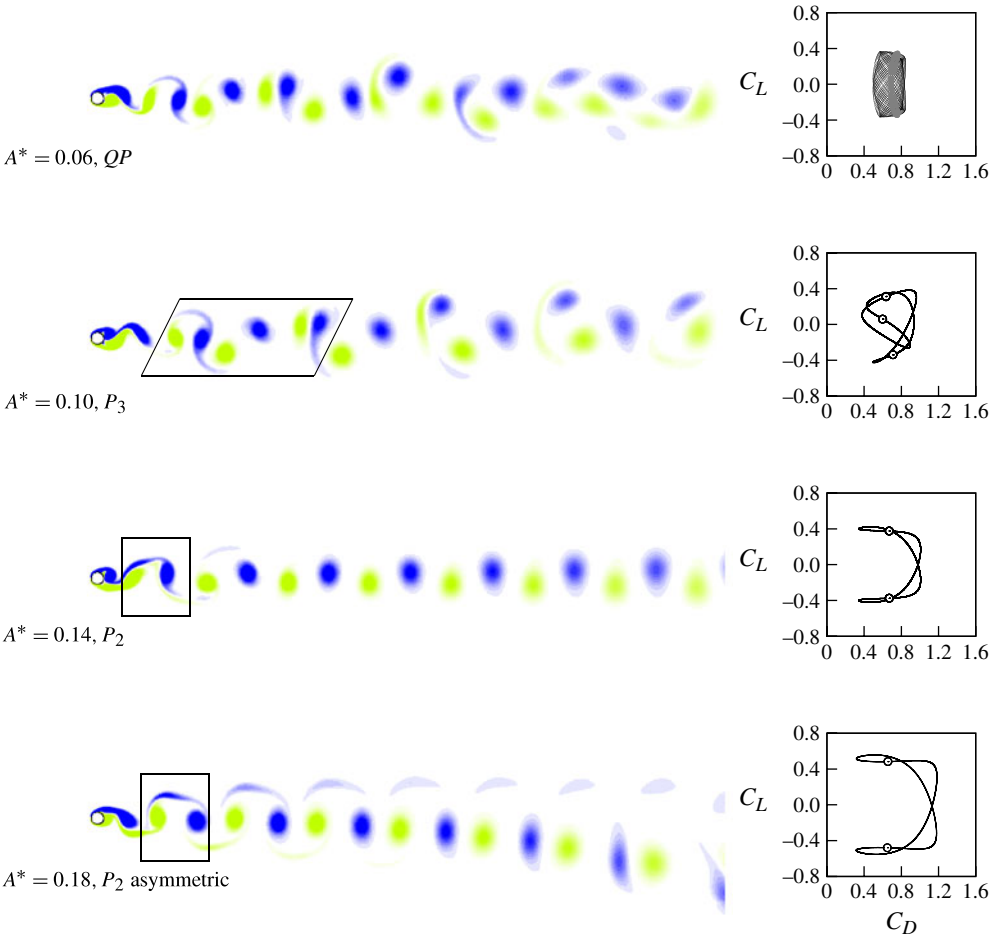

FIGURE 5. (Colour online) Snapshots of vorticity at levels ± 1, and Lissajous plots of lift coefficient C_L against drag coefficient C_D, for $Re = 175$, $f_d/f_{St} = 1.4$, for a series of oscillation amplitudes, increasing from top to bottom. The boxes on the wake images mark the vortices shed over one repetition, or N cylinder oscillations. The points on the Lissajous plots come from sampling the lift and drag once each oscillation period. The data presented are the same as those of figure 6.

oscillation cycles; for $Re = 250$, this represents approximately 207 oscillation cycles. Observation of the time histories of the forces showed most simulations to settle to a statistically stable state by the end of 30 cycles.

Table 1 presents these values of f_{St}, as well as data on the quality of power-law fits to the measured frequencies of vortex shedding as a function of A^*. Columns 3 and 4 of table 1 show the coefficients from a least-squares fit of the form

$$f_s = f_{St} + \alpha A^{*\beta}. \tag{3.1}$$

The exponent of this fit is shown to remain very close to $\beta = 2$, with a maximum deviation from 2 of less than 9 % at $Re = 75$. This further confirms the findings of

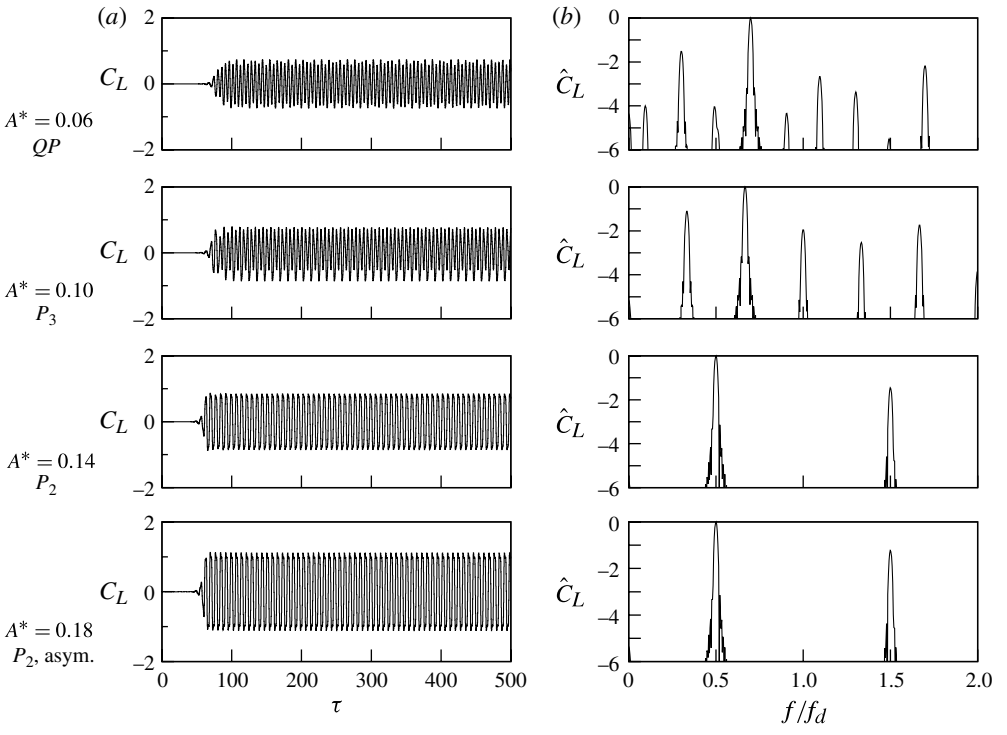

FIGURE 6. (*a*) Time histories of the lift coefficient C_L and (*b*) portions of the frequency spectra obtained from taking the Fourier transform of the lift coefficient history; $Re = 175$, $f_d/f_{St} = 1.4$. The amplitude of oscillation increases from top to bottom. The change in signature of the time history and spectrum as the flow moves from quasi-periodic to the various synchronized modes is clear. The data presented are the same as those of figure 5.

Re	$f_{St} = f_d$	α	β	Γ_{1_2}	R^2_β	R^2_2
75	0.15248	−0.089819	2.166066	−0.080078	0.000007	0.000009
100	0.16788	−0.158521	1.991784	−0.159850	0.000004	0.000004
125	0.17865	−0.260606	2.051223	−0.247340	0.000006	0.000007
150	0.18681	−0.329193	2.000862	−0.328850	0.000006	0.000006
175	0.19312	−0.426272	2.020985	−0.414269	0.000010	0.000010
200	0.19863	−0.521857	2.020914	−0.506055	0.000002	0.000002
250	0.20684	−0.912254	2.148225	−0.704771	$<10^{-6}$	0.000001

TABLE 1. Coefficients for the power-law fits $f_{sp1} = f_{St} + \alpha A^{*\beta}$ and $f_{sp2} = f_{St} + \Gamma_{1_2} A^{*2}$, for varying Re, with $f_d/f_{\mathrm{St}} = 1$. In all cases when the exponent is fitted from the data, the exponent β remains very close to 2. The R^2_β value is defined as $\sum (f_s - f_{sp1})^2$, and similarly for R^2_2, where the subscripts refer to the order of the highest term in the series of the fit. The error in the fit is always of the same order of magnitude, whether the exponent β is fixed to 2 or allowed to vary.

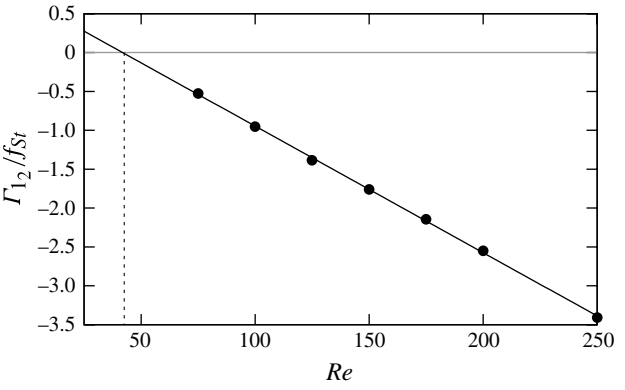

FIGURE 7. Coefficient Γ_{1_2}/f_{St} as a function of Re, $f_d/f_{St} = 1$. The solid black line is a linear fit, $\Gamma_{1_2}/f_{St} = -0.0163Re + 0.683$, to the data points. The match between the measurements and the fit is excellent. Extrapolation of the fit shows that $\Gamma_{1_2} = 0$ at $Re \simeq 42$, indicating that the frequency will cease to decrease with increasing A^* at this value. This value of Re is just below that where vortex shedding from a stationary cylinder begins ($Re \simeq 47$).

Leontini *et al.* (2011) and Tudball-Smith *et al.* (2012) that the frequency of vortex shedding decreases proportionally to A^{*2}, regardless of Re.

Column 5 of table 1 shows the fitting coefficient from a least-squares fit when this exponent is fixed to $\beta = 2$, or (1.1) truncated to the first term (this truncation is reflected in the label for the coefficient, Γ_{1_2}, where the first subscript refers to the term in the series, and the second subscript refers to the order of the term at which the series is truncated). The difference between this column and column 3 (the same coefficient when β is allowed to vary) is minimal, and the quality of the fit to the data is of the same order. This last point is further confirmed by comparing the R^2 values of both the fits in columns 6 and 7. Here, R^2 is defined as $\sum (f_s - f_{sp})^2$, where f_{sp} is the predicted shedding frequency from the fit.

The data in table 1 establish that f_s is proportional to A^{*2}, at least when $f_d/f_{St} = 1$, or that (1.1) can be truncated to the first term. With f_d/f_{St} held fixed, the coefficient of proportionality, Γ_{1_2}, is a function of Re only. Figure 7 plots Γ_{1_2}/f_{St} as a function of Re, and clearly shows a linear variation. A least-squares fit to the data gives the function

$$\Gamma_{1_2}/f_{St} = -0.0163Re + 0.683. \tag{3.2}$$

The fit can be extrapolated back to find where $\Gamma_{1_2}/f_{St} = \Gamma_{1_2} = 0$, or the value of Re where the amplitude of oscillation is expected to have no effect on the vortex shedding frequency. This value is $Re \simeq 42$, and is marked by the dotted line in figure 7. This is just slightly below the value at which vortex shedding from a stationary cylinder begins ($Re \simeq 47$) (Provansal, Mathis & Boyer 1987; Le Gal, Nadim & Thompson 2001). This result appears consistent with the idea that the oscillating body acts as a wavemaker in the flow, with a viscous limit to its operation. The result of $\Gamma_{1_2} = 0$ at $Re \simeq 42$ indicates that, below this Re, the vortex shedding frequency is not influenced by the oscillation. One possible interpretation of this is that the vortex shedding ceases altogether, but this is not necessarily the case.

Further, the fit defined in (3.2) can be substituted directly into the truncated series as defined in (1.2), and combined with $f_d/f_{St} = 1$. This can then be rearranged to arrive at an equation for the amplitude of oscillation as a function of the shedding frequency

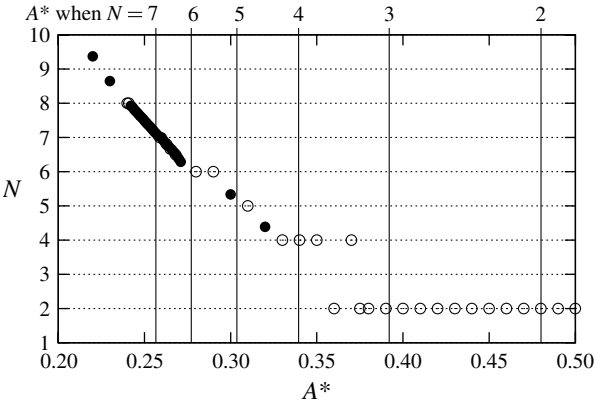

FIGURE 8. Value of N, calculated using (3.4) for the data at $Re = 175$, $f_d/f_{St} = 1$. Closed symbols (•) denote quasi-periodic cases; open symbols (○) denote P_N periodic cases. Vertical lines are amplitudes predicted for a given N using (3.5). The plot shows that the ranges of A^* where the flow synchronizes to a P_N mode are focused around the values of A^* predicted by (3.5). The predicted P_3 mode is not found using simulations started from rest.

and the Reynolds number,

$$A^* = \pm\sqrt{\frac{f_s/f_d - 1}{-0.0163Re + 0.683}}. \tag{3.3}$$

Leontini *et al.* (2011) showed that a series of P_N periodic modes exists, which repeat over N driving periods. These modes occur when the ratio of the driving frequency to the shedding frequency is in the vicinity of an integer, specifically

$$N = \frac{1}{1 - f_s/f_d}. \tag{3.4}$$

When the amplitude of oscillation A^* is such that N is close to an integer ratio, the vortex shedding will synchronize with the driving so that N is exactly an integer ratio. A result of this is that a small range of A^* will exist where N remains locked to an integer.

Equation (3.4) can be rearranged and substituted into (3.3) to give

$$A^* = \pm\sqrt{\frac{-1}{N(-0.0163Re + 0.683)}}. \tag{3.5}$$

Equation (3.5) can then be used to predict the amplitudes of oscillation at which a P_N mode will occur (if the nonlinear synchronization is ignored) as a function of Re, simply by substituting N into the equation. Owing to the nonlinear synchronization process, this amplitude should fall in the range of A^* at which a given P_N mode is observed. This equation shows that, for a given P_N mode, the A^* around which its range is focused varies with $Re^{-1/2}$.

Figure 8 shows N, as defined in (3.4), for $Re = 175$. Cases where the flow was deemed to be quasi-periodic are marked with open symbols, P_N cases are marked with closed symbols. The fact that the closed symbols 'lock' to a given value of N is due to synchronization of the wake to a multiple of the driving frequency. The vertical lines mark the amplitudes at which (3.5) predicts P_N, for $2 \leqslant N \leqslant 7$. The plot shows that the

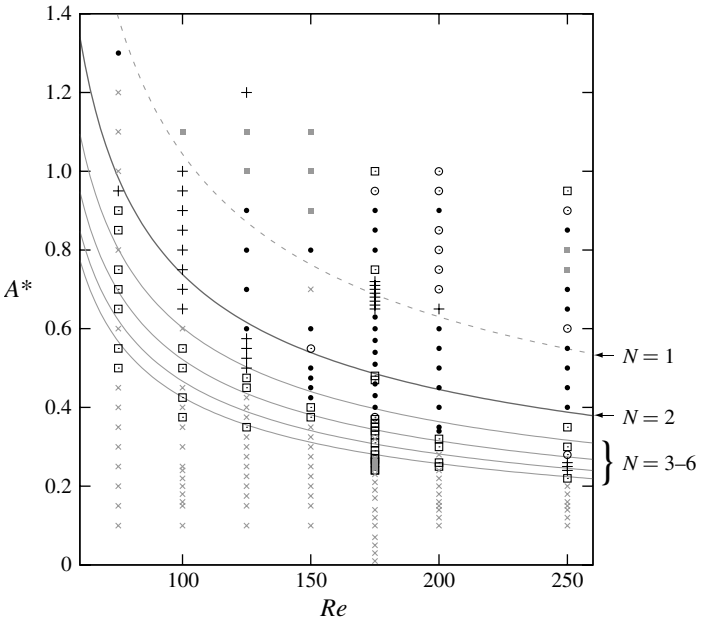

FIGURE 9. Regimes of response as a function of A^* and Re, for $f_d/f_{St} = 1$. Symbols depict different response regimes delineated by their spatial and temporal symmetries: P_2 (•); P_2, non-zero mean lift (○); symmetric shedding (■, grey); chaos (+); P_N other than P_2 (□); quasi-periodicity (×, grey). Some data points for $Re = 175$ have been removed for clarity in areas where a particular mode covered a band of amplitudes. The thick solid grey line marks A^*, as a function of Re, at which the data fits predict $f_s = 0.5f_d$, or $N = 2$, if the effect of nonlinear synchronization is ignored. The onset of the P_2 mode is shown to occur at A^* just prior to this. The dashed line marks A^* at which $N = 1$. The onset of the symmetric shedding mode (for which $f_s = f_d$) is shown to occur close to this line. The thin solid grey lines show where the fits predict the modes P_3–P_6, respectively, with decreasing A^*, as annotated at the right-hand side of the plot.

flow synchronizes to a P_N mode in a range focused at the value of A^* predicted for that N from (3.5).

In the example at $Re = 175$ shown in figure 8, no P_3 mode is obtained from the simulations started from rest. In the region where it is predicted, there appears to be significant overlap with both the P_2 and P_4 modes, indicating that multiple modes can be obtained in this region. A P_3 mode does occur for other values of Re, and it therefore seems likely that its discovery at $Re = 175$ is simply a function of the initial conditions.

Extending this same idea, lines of constant N have been plotted in figure 9, along with a map of the states obtained from simulations. The flow states have been broken down into categories according to their spatial and temporal symmetry properties. The major classes are P_2 periodic, P_N periodic, quasi-periodic, chaotic and a symmetric mode. The P_2 periodic mode can be further divided into zero and non-zero mean lift modes, corresponding to different wake configurations.

Figure 9 shows that the flow states obtained do follow the trends predicted by the constant N lines of (3.5). The clearest evidence of this is the onset of the P_2 mode. For $Re \leqslant 125$, the onset of the P_2 mode is shown to occur just below the solid line

representing A^* when $N = 2$. The reason for the onset occurring below the line is that nonlinear synchronization 'locks' the flow to the periodic mode over a range of A^*.

For $Re < 125$, the onset of the P_2 mode is not observed near the predicted value of A^*, instead replaced with chaotic or quasi-periodic responses. It is hypothesized that this chaotic response is due to mode competition between the P_2 mode and the symmetric shedding mode that occurs at higher A^*. It is also possible that multiple modes are possible at any given point in the parameter space, with the transitions between different regimes being hysteretic. The purpose here is not to provide an exhaustive map of states; rather, it is to try to uncover the important aspects of the system that give rise to the dynamics. The map shown in figure 9 shows that the P_N periodic modes occur in the regions predicted by synchronization between the shedding and driving frequencies. It also shows that, when chaos occurs, it occurs in 'overlap' regions between modes (such as between P_2, P_3 and P_4 modes, or between the P_2 mode and the symmetric mode), indicating that it is due to mode competition.

Also plotted on figure 9 is a dashed line indicating where $N = 1$. Equation (3.4) shows that this corresponds to $f_s/f_d = f_s = 0$. Recalling that the oscillating body is being treated as a wavemaker, $N = 1$ therefore predicts the amplitude at which the vortex shedding process is completely supplanted by the oscillation, and any oscillation in the flow would be purely due to the driving. It also indicates that there is no competition or interaction between waves and the driving, and so it might be expected that the symmetry of the flow would match the symmetry of the driving. Figure 9 shows that the onset of the symmetric shedding mode, when it is observed, occurs reasonably close to this $N = 1$ line. This is particularly clear for $100 \leqslant Re \leqslant 150$. The symmetric mode is synchronized with the driving frequency, and shares the symmetry of the forcing. It therefore seems that the appearance of the symmetric mode is due to the oscillation no longer being a perturbation on top of the natural vortex shedding process, but being so large that it completely overwhelms the flow and controls the response, meaning that the flow responds purely to the driving.

3.2.1. *Influence of parameters on wake configuration*

The parameter space map of figure 9 essentially identifies regimes by their temporal behaviour. However, even for flows with the same temporal behaviour, the wake configuration can be significantly different. This is most easily understood in terms of spatio-temporal symmetries. For instance, the standard Kármán vortex street or $2S$ wake mode (consisting of two single vortices shed per period) has a spatio-temporal symmetry of evolution forward in time by half a period combined with reflection about the wake centreline, or $u(x, y, t) = u(x, -y, t + T/2)$. On the other hand, the $P + S$ wake mode (consisting of a single vortex on one side, and an opposite-signed pair on the other side) does not possess this symmetry.

For the parameter space of figure 9, there are a number of organized wake modes. In particular, the P_4 and P_2 modes can be found in spatio-temporally symmetric and asymmetric configurations. Figure 10 presents snapshots of the wake over the parameter range $0.15 \leqslant A^*$, and $75 \leqslant Re \leqslant 250$, as well as the case of the unperturbed cylinder for each Re. The variation in wake configurations is striking. For small A^*, the flow resembles the classic Kármán vortex street. With increasing A^*, the modulation of the wake and quasi-periodicity are clear, with the wake 'wandering' from side to side. With further increases in A^* (which results in lowering f_s according to (3.1), and therefore a lowering of N according to (3.4)), P_N modes occur.

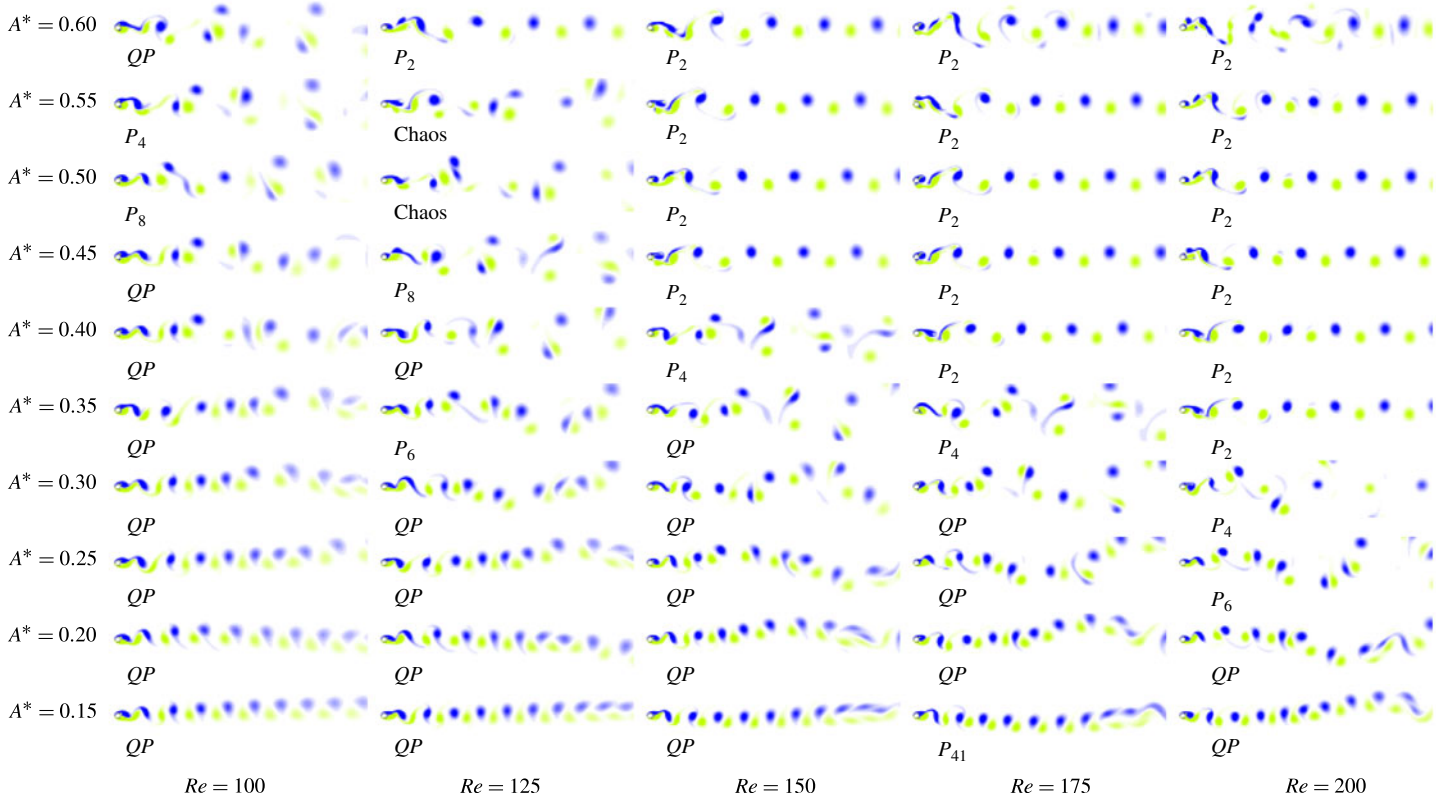

FIGURE 10. (Colour online) Snapshots of the wakes produced by the oscillating cylinder when $f_d/f_{St} = 1$, visualized using vorticity contours at levels between ± 1. Reynolds number increases from left to right; amplitude of oscillation increases from bottom to top. The labels under each image designate the temporal behaviour of the flow. The increased complexity of the wake as the flow approaches the point where locking to the P_2 mode or chaos is observed is clear (cutting an approximately diagonal path from the top left to the bottom right of the figure). A wide variety of wake modes are shown. Different configurations of vortices for the same temporal behaviour are possible: see, for example, the P_2 modes at $Re = 200$, $A^* = 0.55$, then $Re = 200$, $A^* = 0.60$, then $Re = 250$, $A^* = 0.60$.

Figure 10 makes it clear that there is a wide range of organized wake modes, and it seems that a number of them are bistable, the mode selected being a function of the initial conditions. The widest variety exists for the P_2 and P_4 modes.

For example, consider the two examples of P_2 modes shown for ($Re = 200, A^* = 0.55$), and ($Re = 200, A^* = 0.60$). The first of these points shows a 'classic' P_2 wake, which maintains a spatio-temporal symmetry similar to the Kármán vortex street, $u(x, y, \tau) = u(x, -y, \tau + T)$, where T is the period of the driving. A single vortex is shed on one side of the wake in one period, and then a single vortex of the opposite sign is shed from the other side in the next period. Over the period of shedding (two periods of the driving), this could be considered a $2S$ mode, following the naming convention of Williamson & Roshko (1988).

The second of these points shows a wake with the same spatio-temporal symmetry as the first, but the configuration of vortices in the wake is different. Near the body, a pair of same-signed vortices is shed from one side during one driving period, then another pair of same-signed vortices (but of opposite sign to the previous pair) is shed from the other side during the next driving period. Downstream, these pairs amalgamate and the wake once again takes on the typical Kármán configuration. The $2P$ wake mode identified by Williamson & Roshko (1988) consists of two pairs of oppositely signed vortices per cycle, and so the mode found here cannot be given the same designation.

Forcing at higher amplitudes, or higher Re, can also lead to a P_2 mode, which results in a non-zero mean lift, breaking the spatio-temporal symmetry. These flows typically manifest as a $P + S$ type wake mode, with a single vortex shed during one oscillation cycle, and an opposite-signed pair shed during the next cycle. Figure 9 shows that these types of flows were observed for $A^* \geqslant 0.9$ for $Re = 200$, and at $A^* = 0.6$ for $Re = 250$.

3.3. *Dependence on f_d/f_{St} when Re is fixed*

This section reports on simulations where the Reynolds number $Re = 175$, but the driving frequency has been varied over the range $0.8 < f_d/f_{St} < 2.0$. Similar to the results of § 3.2, all the simulations were started from rest and run up to $\tau = 1000$.

Table 2 presents the coefficients of a series of power-law fits to the measured vortex shedding frequencies as a function of A^*. Three fits are considered. First, the coefficients of a fit where the exponent is free to float, of the form shown in (3.1), are presented in columns two and three. Second, the single coefficient of the series in A^{*2} presented in (1.1) truncated to the first term is presented in column four. Third, the coefficients of the same series truncated to two terms are presented in columns five and six. These truncations are reflected in the label for the coefficients, Γ_{1_2}, Γ_{1_4} and Γ_{2_4}, where the first subscript refers to the term in the series, and the second subscript refers to the order of the term at which the series is truncated. Columns seven to nine present an estimate of the quality of each of the three fits.

The R^2 values presented in table 2 show that, for values of $f_d/f_{St} \simeq 1$, the series truncated to a single term gives a fit that is as good as the more complicated fits. However, as f_d/f_{St} is either decreased or increased, the single-term fit in A^{*2} is not as good as the general power-law fit or the series extended to two terms.

For higher values of f_d/f_{St} it is proposed that higher order terms are required for an accurate fit, as the range of A^* over which the general decrease in f_s before synchronization to the P_2 mode occurs becomes shorter with increasing f_d/f_{St}. Even at amplitudes just below those at which full synchronization occurs, the physical process that leads to the vortex shedding slowing down (as required for synchronization) is

f_d/f_{St}	α	β	Γ_{1_2}	Γ_{1_4}	Γ_{2_4}	R^2_β	R^2_2	R^2_4
0.80	−1.233411	2.896474	−0.351561	−0.166604	−2.947582	3.451×10^{-6}	3.862×10^{-5}	1.571×10^{-6}
0.90	−3.142298	3.205738	−0.346451	−0.122112	−8.567235	5.324×10^{-7}	8.369×10^{-6}	2.621×10^{-7}
0.95	−0.423819	2.299630	−0.297407	−0.243770	−0.540265	2.112×10^{-6}	1.220×10^{-5}	1.880×10^{-6}
1.00	−0.426272	2.020985	−0.414269	−0.410360	−0.057856	1.006×10^{-5}	1.024×10^{-5}	1.014×10^{-5}
1.05	−0.709560	2.241162	−0.483239	−0.422694	−1.378006	2.226×10^{-6}	6.322×10^{-6}	3.606×10^{-6}
1.10	−0.679061	2.144739	−5.464505	−0.502547	−0.792820	3.848×10^{-6}	7.345×10^{-6}	5.203×10^{-6}
1.20	−1.250721	2.259251	−0.770192	−0.654689	−4.529764	7.999×10^{-7}	4.352×10^{-6}	1.570×10^{-6}
1.40	−3.650789	2.401517	−1.342931	−1.023967	−45.43213	2.255×10^{-8}	5.852×10^{-7}	6.737×10^{-8}
1.60	−22.44115	2.761556	−2.855162	−1.569801	−282.2914	9.681×10^{-7}	9.583×10^{-6}	4.045×10^{-7}
1.70	−29.60988	2.670056	−3.708277	−2.226549	−713.7022	6.859×10^{-8}	1.694×10^{-6}	2.112×10^{-8}
1.80	−339.6341	3.146358	−6.360128	−2.354444	−4052.954	2.164×10^{-7}	3.960×10^{-6}	1.044×10^{-7}
1.90	−675.4416	2.970021	−10.26021	−4.529985	−31177.29	2.915×10^{-8}	2.896×10^{-7}	4.811×10^{-8}

TABLE 2. Coefficients for the power-law fits $f_{sp1} = f_{St} + \alpha A^{*\beta}$, $f_{sp2} = f_{St} + \Gamma_{1_2} A^{*2}$ and $f_{sp3} = f_{St} + \Gamma_{1_4} A^{*2} + \Gamma_{2_4} A^{*4}$ for varying f_d/f_{St}, with $Re = 175$. The R^2_β value is defined as $\sum (f_s - f_{sp1})^2$, and similarly for R^2_2 and R^2_4, where the subscripts refer to the order of the highest term in the series of the fit.

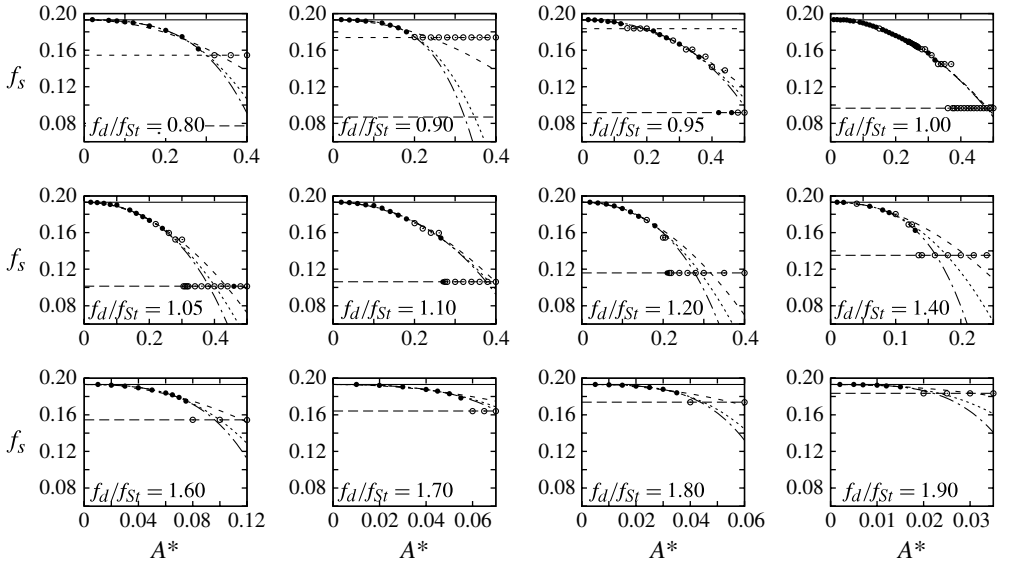

FIGURE 11. Vortex shedding frequency f_s as a function of A^* for all the frequency ratios f_d/f_{St} tested. Quasi-periodic responses are marked with closed circles; other response types are marked with open circles. The solid horizontal line marks f_{St}, the short-dashed horizontal line marks the driving frequency f_d when $f_d/f_{St} < 1$, and the long-dashed horizontal line marks f_d. The frequency axis is the same for all the plots; the amplitude axis is scaled to show the region of interest. Three different fits are shown to the data: $f_s = f_{St} - \alpha A^{*2}$ (long-dashed), $f_s = f_{St} - \alpha A^{*\gamma}$ (short-dashed), and $f_s = fst - \alpha A^{*2} - \beta A^{*4}$ (dash-dotted). While the more complex fits fit the quasi-periodic data better, the plain A^{*2} fit seems to give a better qualitative indication of the pure vortex shedding and wavemaking process, as it passes through somewhere near the centre of the P_2 region. The f_d/f_{St} value increases from left to right, and from top to bottom.

operating, and so a higher-order correction is required. As the range of A^* before synchronization is very short, proportionally the range of A^* over which this higher-order correction is required is larger, hence the increasing influence of higher-order terms.

However, qualitatively, the single-term fit appears to give a better representation of the underlying behaviour. Figure 11 shows f_s as a function of A^* for values of f_d/f_{St} from $f_d/f_{St} = 0.80$ to $f_d/f_{St} = 1.9$. Also plotted are curves representing the three fits whose coefficients are presented in table 2. In cases where there is a significant difference between the fits, the fit in A^{*2} (the series truncated to a single term) is flatter, and appears to pass through $f_s = f_d/2$ at an amplitude further above that at which synchronization to the P_2 mode first occurs.

This seems to indicate that the underlying physics is still dominated by the first term of the series of (1.1), and f_s varies with A^{*2}. Following this truncation, the data can be analysed in a similar fashion to the constant-f_d/f_{St}, varying-Re data of § 3.2. Figure 12 shows the coefficient of this single-term fit as a function of f_d/f_{St}. Two important features of this plot are apparent. The first is that, for $f_d/f_{St} \geqslant 1$, there is a rapid decrease in the coefficient as $f_d/f_{St} \to 2$. The second is the fact that the coefficient is almost constant for $f_d/f_{St} < 1$. This suggests that the dependence of f_s on f_d/f_{St} is of a different form depending on whether $f_d/f_{St} \geqslant 1$ or not.

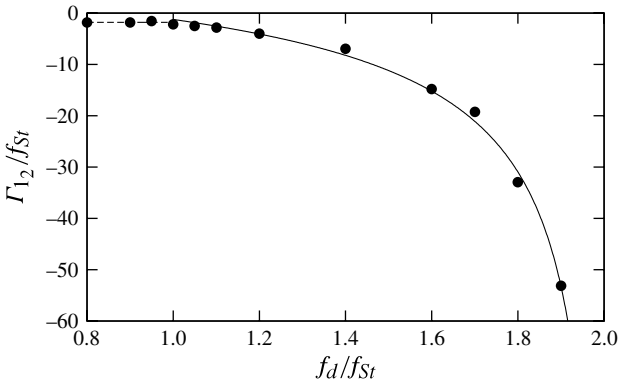

FIGURE 12. Coefficient Γ_{1_2}/f_{St} as a function of f_d/f_{St}, $Re = 175$. The solid line is a fit of the form of (3.7) to the data for $f_d/f_{St} \geqslant 1$. The dashed line shows that the trend of the coefficient Γ_{1_2} is essentially constant for $f_d/f_{St} < 1$.

For the cases where $f_d/f_{St} \geqslant 1$, the rapid decrease in Γ_{1_2} as $f_d/f_{St} \to 2$ indicates that there is a vertical asymptote at $f_d/f_{St} = 2$. Physically, this means that any relationship between f_s and A^* of the form defined in (1.2) is only valid for $f_d/f_{St} < 2$. This is perhaps not surprising, as, at $f_d/f_{St} = 2$, 'synchronization' to a P_2 mode consists of the frequency f_s being unaffected by the amplitude of oscillation. This asymptote suggests that the relationship between the coefficient and f_d/f_{St} is of the form

$$\Gamma_{1_2} = C_1/(2 - f_d/f_{St})^{C_2} + C_3, \tag{3.6}$$

where C_1, C_2 and C_3 are real coefficients. Fitting a curve of this form to the data plotted in figure 12 for $f_d/f_{St} \geqslant 1$ (also shown in column four of table 2), gives a power $C_2 \simeq 0.55$. If this power is fixed to $C_2 = 0.5$, then (3.6) becomes

$$\Gamma_{1_2} = \frac{-4.6457}{\sqrt{2 - f_d/f_{St}}} + 4.4074. \tag{3.7}$$

This fit is represented by the solid line in figure 12.

Similar to the process employed in § 3.2, this equation can be substituted back into the truncated series for f_s and combined with (3.4) and the definition of f_d/f_{St}, then rearranged to solve for the value at A^* at which a P_N mode is 'predicted', if the nonlinear synchronization effects are ignored. Following this process gives the equation

$$A^* = \sqrt{\frac{[(1 - N^{-1})f_d/f_{St} - 1]f_{St}}{-4.6457/\sqrt{2 - f_d/f_{St}} + 4.4074}}. \tag{3.8}$$

For $f_d/f_{St} < 1$, the picture is much simpler, in that the coefficient Γ_{1_2} appears essentially independent of f_d/f_{St}, remaining at a constant value of $\Gamma_{1_2} \simeq 0.35$. This can also be used to predict the amplitude at which a given P_N mode will occur using

$$A^* = \sqrt{\frac{[(1 - N^{-1})f_d/f_{St} - 1]f_{St}}{-0.35}}. \tag{3.9}$$

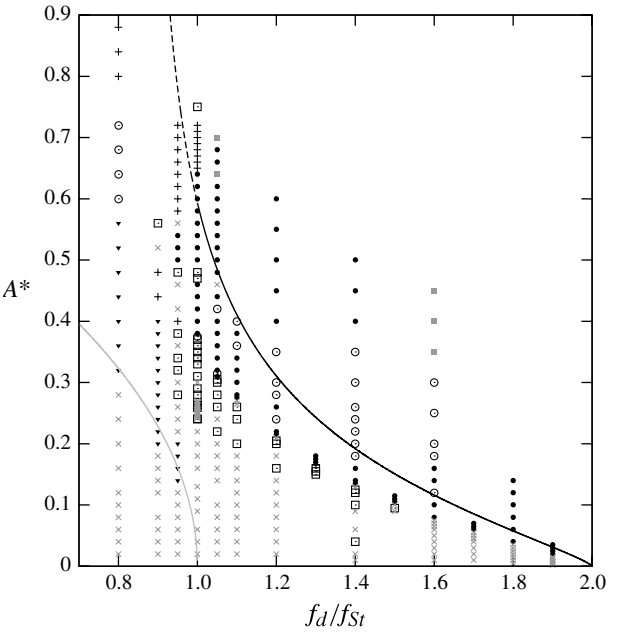

FIGURE 13. Regimes of response as a function of A^* and f_d/f_{St}, for $Re = 175$. Symbols depict different response regimes delineated by their spatial and temporal symmetries: P_1 (▼); P_2 (●); P_2, non-zero mean lift (○); symmetric shedding (■, grey); chaos (+); P_N other than P_1 or P_2 (□); quasi-periodicity (×, grey). Similar to figure 9, some data points have been removed for $f_d/f_{St} = 1$ from continuous bands for clarity. The solid black line represents the amplitude for which (3.8) predicts that the vortex shedding frequency will reach $f_d/2$, or $N = 2$. It falls just above where the P_2 mode is first observed. The dashed black line represents the continuation of (3.8), predicting the same amplitude, below $f_d/f_{St} = 1$. The grey line represents the amplitude at which it is predicted that $f_s = f_d$. It falls just above where the P_1 mode is first observed.

A parameter space map of flow states as a function of f_d/f_{St} and A^* is presented in figure 13. Similar to figure 9, the flow states are grouped into five categories based on their temporal and spatial properties: P_2 periodic, P_N periodic, quasi-periodic, chaotic, and a symmetric mode. The P_2 periodic modes are further divided into zero and non-zero mean lift modes. This last distinction is important especially when considering flows where $f_d/f_{St} < 1$, and will be expanded upon below.

The closed black circles of figure 13 show where the P_2 mode was observed. It is clear that, as f_d/f_{St} is increased, the amplitude at which the P_2 mode is first observed decreases. The solid black line represents (3.8), with $N = 2$; for $f_d/f_{St} \geqslant 1$, it consistently falls at amplitudes above those at which the P_2 mode is first observed.

Observation of this curve and inspection of (3.8) shows that the amplitude at which the P_2 mode is expected decreases towards $A^* = 0$ as $f_d/f_{St} \to 2$. However, A^* for the P_2 mode rapidly increases as f_d/f_{St} is decreased from $f_d/f_{St} = 1$, marked by the dashed black line on figure 13. Note that this equation is defined from a fit to data only over the range $f_d/f_{St} \geqslant 1$, and so is only strictly valid in this region. However, some interesting conclusions can be drawn from extrapolating this curve back. The derivative of (3.8), $\partial A^*/\partial(f_d/f_{St})$, is undefined at $f_d/f_{St} \simeq 0.81$, indicating an asymptote of the curve at this value. This suggests that there are no real values of A^* for

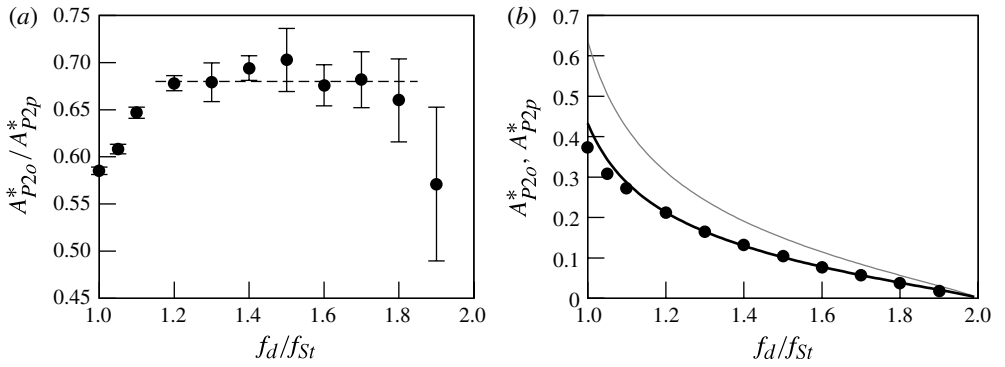

FIGURE 14. Determination of the boundary of onset of the P_2 mode as a function of A^* and f_d/f_{St}. (*a*) The ratio between A^*_{P2o}, the lowest amplitude where the P_2 mode is observed, and A^*_{P2p}, the amplitude where the P_2 mode is 'predicted' to occur by (3.8). The upper error bars mark the amplitude where the P_2 mode is observed; the lower error bars mark the next lowest amplitude at which simulations were conducted; the points (•) mark the average of these two. The ratio between 'prediction' and observation settles to an almost constant value of around 0.68 over a wide range of f_d/f_{St}. (*b*) Plots of A^*_{P2p} (thin grey line), $0.68A^*_{P2p}$ (thick black line) and A^*_{P2o} (•). The approximation of the P_2 onset boundary by the black line tracks the observed transition quite closely over most of the range of f_d/f_{St} tested.

$f_d/f_{St} < 0.81$ at which the P_2 mode occurs, at least not through the same shedding process as for $f_d/f_{St} \geqslant 0.81$. In fact, this asymptote exists regardless of the value of N, and so it suggests that the underlying dynamics is different for $f_d/f_{St} < 0.81$.

Figure 13 also shows that the P_2 mode is observed at values of A^* below the value where is it 'predicted' by (3.8). This is expected, as (3.8) only accounts for the lowering of the frequency by the oscillation, and not the nonlinear synchronization. The nonlinear synchronization process takes over as the vortex shedding frequency f_s gets into the vicinity of $f_d/2$ as f_s is lowered by the increasing amplitude A^*. The data presented in figure 14 attempt to quantify this effect.

Figure 14(a) shows the ratio between A^*_{P2o}, the lowest observed amplitude at which the P_2 mode occurs for a given f_d/f_{St}, and A^*_{P2p}, the amplitude at which the P_2 mode is 'predicted' to occur by (3.8). The figure shows that, over most of the range of f_d/f_{St} tested, this ratio is almost constant at a value of around 0.68. Figure 14(*b*) then plots A^*_{P2p}, along with $0.68A^*_{P2p}$, and the observed A^*_{P2o}. The figure shows that simply multiplying A^*_{P2p} by a factor provides a very reasonable approximation of the location of the P_2 onset boundary, especially for $f_d/f_{St} > 1.2$. Therefore, the location of this boundary for $1 \leqslant f_d/f_{St} \leqslant 2$ is approximately

$$A^* = 0.68\sqrt{\frac{(0.5f_d/f_{St} - 1)f_{St}}{-4.6457/\sqrt{2 - f_d/f_{St}} + 4.4074}}, \tag{3.10}$$

which is simply (3.8) with $N = 2$ multiplied by 0.68. Note that (3.10) does not come from fitting the location of the P_2 onset boundary directly, but rather comes from considering Γ_{1_2}, the rate at which the vortex shedding frequency decreases with increasing amplitude.

It should be highlighted here that this result supports the conclusion that there are two important processes occurring that ultimately influence the frequency selection and the onset of the P_2 mode. The first is the lowering of the vortex shedding frequency

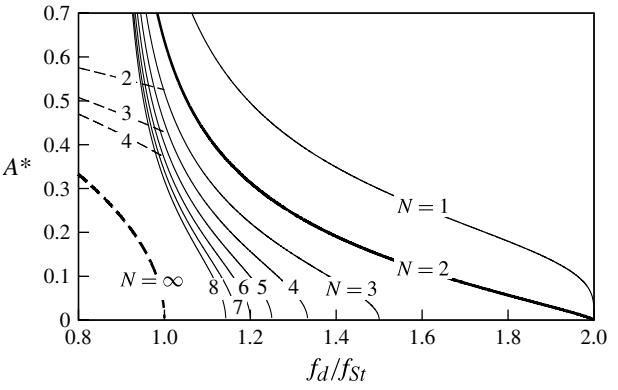

FIGURE 15. A schematic showing contours of N calculated from (3.8) for $f_d/f_{St} > 1$ marked with solid lines and from (3.9) for $f_d/f_{St} \leqslant 1$ marked with dashed lines. Each line gives some indication of the region of parameter space where each P_N mode is expected to occur. Nonlinear synchronization will act to lock the flow to the corresponding P_N mode in the vicinity of each curve. Note that $N = \infty$ corresponds to the case where $f_s = f_d$, or a P_1 mode. The solid lines also show that the number of P_N modes accessible reduces as f_d/f_{St} is increased.

by the increased amplitude of oscillation. The second is the nonlinear synchronization when this lowered vortex shedding frequency moves into the vicinity of $f_d/2$. Hence (3.8) does not predict the lowest amplitude at which the P_2 mode will occur, but rather predicts an amplitude that will be bracketed by the lowest and highest amplitudes of the P_2 mode (in fact, the same can be said for any P_N mode). The data presented in figure 14 give some indication as to when the simple trend of f_s varying with A^{*2} will be overridden by the nonlinear synchronization.

Keeping in mind that synchronization will act to realize P_N modes at amplitudes both higher and lower than those predicted by (3.8) and (3.9), some idea of the regions of parameter space where each P_N mode can be expected can be gained by plotting contours of constant N. Such a plot is presented in figure 15.

Concentrating on the contours in the range $1 < f_d/f_{St} < 2$, the main point to be drawn from the plot is that the number of P_N modes accessible reduces as f_d/f_{St} is reduced, regardless of the amplitude of oscillation. This fits with the observations presented in figure 13. A consequence of this is that, at values of f_d/f_{St} near to, but greater than, unity, a very large range of locked states is possible depending on amplitude.

The contours for $f_d/f_{St} \leqslant 1$ also show that a number of P_N states are possible. Combining these observations, it is clear that, for values of f_d/f_{St} near unity, and amplitudes $0.4 < A^* < 0.55$, there is a very large population of locked states coming from both sides of $f_d/f_{St} = 1$. Therefore, the final state selected by the flow in this region of the parameter space is probably a function of the initial conditions, and mode competition becomes more likely. This suggests that experiments using parameters in this region may be susceptible to very small changes, and difficult to control.

The picture presented in figure 15 shows that the dynamics of the wake is very rich, with overlapping areas of synchronization, and highly asymmetric regions of synchronization in terms of f_d/f_{St}. The presence of the $N = 1$ contour, which possibly gives some indication of the amplitude at which the 'natural' vortex shedding is

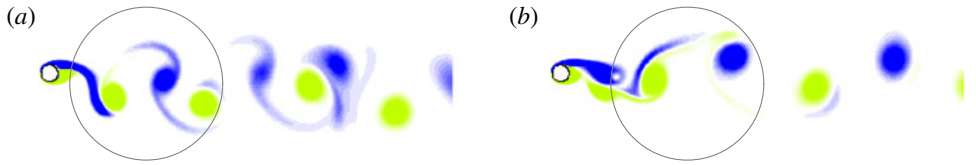

FIGURE 16. (Colour online) A comparison of the wake structures at (*a*) $f_d/f_{St} = 0.8$, $A^* = 0.60$, and (*b*) $f_d/f_{St} = 1.0$, $A^* = 0.40$. Both panels show vorticity contours between levels ± 1. Both are synchronized to a frequency $f_d/2$, or a P_2 mode. The circles mark the vortices shed over two periods of oscillation. The difference in structure is evident: the $f_d/f_{St} = 0.8$ case consists essentially of a pair of vortices being shed in each period (one from each side of the cylinder), each subsequent pair being slightly different from the previous pair; whereas the $f_d/f_{St} = 1.0$ case consists of a vortex from one side in one period, then a vortex from the other side in the next period.

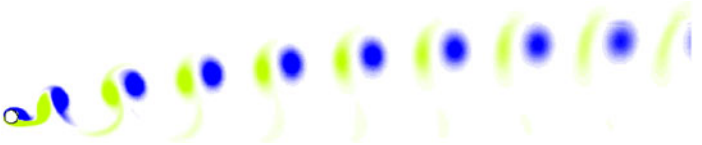

FIGURE 17. (Colour online) A snapshot of vorticity contours at levels between ± 1 showing the P_1 mode at $f_d/f_{St} = 0.80$, $A^* = 0.40$. The vortex shedding process is similar to that for the stationary cylinder, except that one vortex is shed on the upstroke of the cylinder, and one on the downstroke of the cylinder, leading to different strength vortices on either side, and hence a non-zero mean lift.

completely supplanted by the forcing, also indicates that there is an upper limit to all the regions of synchronization, as above this limit there is no vortex shedding frequency for the driving to synchronize. It is therefore not trivial to describe the streamwise forcing of the wake in terms of simple forced oscillators, particularly if a single oscillator model is to be used over the whole parameter space.

Some general comparisons can be drawn. At low amplitudes, the series of constant N contours meeting the f_d/f_{St} axis shown in figure 15 could be thought of as representing a series of Arnol'd tongues (Arnol'd 1965), which consist of regions of synchronized response interleaved with regions of quasi-periodicity, first described for the circle map. It may be informative to attempt to model this problem in such a way, empirically constructing a map and analysing its properties in a dynamic systems sense. Such modelling is left for future work.

Figure 13 shows that a P_2 mode is observed for $f_d/f_{St} = 0.80$, albeit one with a non-zero mean lift, regardless of A^*. This is in contrast to all the other values of f_d/f_{St} at which the P_2 mode is observed, where the lowest A^* for the P_2 mode saw a mode with a zero mean lift observed. Figure 16 shows snapshots of the wake for $f_d/f_{St} = 0.80$, $A^* = 0.60$, and $f_d/f_{St} = 1.0$, $A^* = 0.40$. Both cases are close to the lowest amplitude at which the P_2 mode is observed for the corresponding value of f_d/f_{St}.

The difference between the two cases is evident. For the $f_d/f_{St} = 0.80$ case, two vortices are shed from the cylinder per oscillation cycle, one from each side of the cylinder. The strengths of these vortices is unbalanced, hence the non-zero mean lift. Also, each subsequent pair of vortices is different from the previous pair, hence the repetition over two oscillation cycles. For the $f_d/f_{St} = 1.0$ case, the vortex shedding is a 'classic' P_2 mode, with one vortex shed from one side of the cylinder during one

oscillation cycle, and another single vortex shed from the other side of the cylinder on the next oscillation cycle.

Another major feature of figure 13 is the emergence of a P_1 mode for $f_d/f_{St} < 1$, represented by the black upside-down triangles. This mode can only occur for $f_d/f_{St} < 1$. When $f_d/f_{St} < 1$, the basic behaviour of the wake is the same as for any other f_d/f_{St}, in that increasing the amplitude of oscillation from $A^* = 0$ sees the frequency of shedding f_s decrease from f_{St}. However, when $f_d/f_{St} < 1$, then $f_d < f_{St}$, and this means that, at some amplitude, $f_s = f_d$. From (3.4), when $f_{St} \to f_d$, $N \to \infty$ (as the two frequencies are identical, the results as $N \to \infty$ could be interpreted as meaning the two components are synchronized over an arbitrary period). This result can be used in (3.9) to predict the amplitude at which the P_1 mode is expected. The grey solid line in figure 13 shows this relationship, and is shown to fall at amplitudes just above where the P_1 mode is first observed. This same relationship is shown by the heavy dashed line in figure 15. The conclusion that the P_1 mode should occur at values of $f_d/f_{St} \leqslant 1$ is consistent with the experimental observations of Cetiner & Rockwell (2001) at higher Re than those considered here.

Figure 17 shows a snapshot of the wake at $f_d/f_{St} = 0.80$, $A^* = 0.40$, representative of the structure of the P_1 mode. It shows that the vortex formation and shedding process is similar to that for the unperturbed cylinder. However, two vortices are shed per oscillation cycle, one from each side of the cylinder. This means that one vortex is shed on the upstroke of the cylinder (when the cylinder is travelling upstream), and one vortex is shed on the downstroke of the cylinder. Because of this difference in the direction of travel of the cylinder, the vortices formed are of unequal strength, and therefore a non-zero mean lift is produced.

This non-zero mean can be considered a direct consequence of the difference in symmetry between the forcing and the unperturbed cylinder wake. The unperturbed wake has a spatio-temporal symmetry, $u(x, y, t) = u(x, -y, t + T/2)$. The forcing, however, has a spatial symmetry, $u(x, y, t) = u(x, -y, t)$, and a temporal symmetry (simply periodicity), $u(x, y, t) = u(x, y, t + T)$. Adding this forcing to the unperturbed wake must break the spatio-temporal symmetry, and only the temporal symmetry (periodicity) is maintained.

Figure 13 also shows that, for some values of f_d/f_{St}, symmetric modes are observed. Similar to the varying Re study presented in figure 9, the symmetric modes observed occur in regions of the parameter space where $N \simeq 1$, or where f_s is predicted to be equal to zero.

3.4. *Comparison with existing results*

While the focus of this paper is to highlight the many complex flow states possible in the case of a streamwise oscillating cylinder, and to show that these states all stem from the same root causes, a comparison of the range of synchronization found, particularly for the P_2 mode, can be made with existing results. The data plotted in figure 14, along with the curve generated from (3.10), are plotted along with the location of this synchronization boundary from a series of previous studies in figure 18. These studies include those conducted numerically and experimentally, as well as those where the cylinder is oscillated and those where an oscillatory component is added to the inflow.

As pointed out by Konstantinidis *et al.* (2003), the data can essentially be split into two groups, those where $Re \leqslant 350$ and those where $Re > 350$. Figure 18 shows a close agreement between the various lower Re datasets and the observed data-predicted

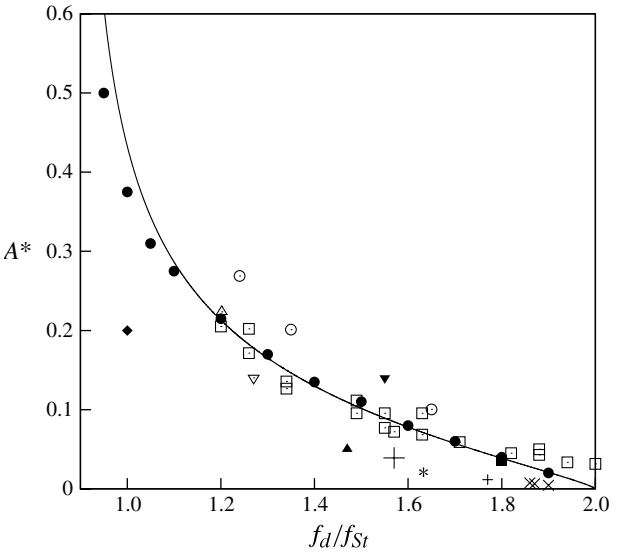

FIGURE 18. The location of the onset of the P_2 mode, from studies across a series of Reynolds number. The solid black line represents the fit from (3.10). Data points are results from: the present study, $Re = 175$ (•); Tanida *et al.* (1973), $Re = 80$ (▽); Tatsuno (1972), $Re = 100$ (○); Konstantinidis & Bouris (2010), $Re = 180$ (△); Griffin & Ramberg (1976), $Re = 190$ (□); Konstantinidis *et al.* (2003), $Re = 2150$ (+); Konstantinidis & Liang (2011), $Re = 2580$ (∗); Barbi *et al.* (1986), $Re = 3000$ (■); Tanida *et al.* (1973), $Re = 4000$ (▼); Nishihara, Kaneko & Watanabe (2005), $Re = 17\,000$ (▲); Jarża & Podolski (2004), $Re = 30\,000$ (+); Armstrong, Barnes & Grant (1986), $Re = 21\,500$ (×); Barbi *et al.* (1986), $Re = 40\,000$ (♦). There is a close agreement between all the cases for $Re < 200$ (open symbols) and the observation and prediction of the present study.

transition boundary from the present study. There is an obvious discrepancy with the results at higher Re, but this is consistent with other lower Re studies.

4. Concluding remarks

It has been shown that the basic response of the cylinder wake to streamwise forcing is similar, regardless of Re and f_d/f_{St}. This response is driven by two root causes: the primary frequency of vortex shedding f_s is lowered proportionally to A^{*2}; and nonlinear synchronization causes the flow to lock to a periodic flow when this lowered vortex shedding frequency is in the vicinity of making a neat ratio with the driving frequency.

The constant of proportionality Γ_{1_2} of the relationship between f_s/f_{St} and A^{*2} has been shown to be a linear function of Re. Extrapolation of this relationship finds that f_s ceases to be a function of A^* when $Re \simeq 42$, predicting that vortex shedding frequency ceases to be controlled by the oscillation at this point. This is very close to the point at which vortex shedding ceases for the unperturbed cylinder, $Re \simeq 47$.

The constant of proportionality Γ_{1_2} between f_s and A^{*2} has been shown to vary with $1/\sqrt{2 - f_d/f_{St}}$, for $1 \leqslant f_d/f_{St} < 2$. At $f_d/f_{St} = 2$, this relationship is undefined, indicating a distinct change in the governing parameters of the vortex shedding. This change coincides with the frequency of forcing at which zero (or vanishing) amplitude is required for synchronization. For $f_d/f_{St} < 1$, the constant of proportionality appears to be unaffected by f_d/f_{St}, taking a constant value of $\Gamma_{1_2} \simeq 0.35$.

The definition of Γ_{1_2} as a function of Re and f_d/f_{St} allows the amplitudes of oscillation at which P_N modes (modes where the vortex shedding is synchronized to N periods of the forcing) occur to be predicted if nonlinear effects are initially ignored. These predictions fall in the range of each observed synchronization. At least for the case where f_d/f_{St} is varied, this linear prediction can be simply corrected by multiplication by a constant factor, to render a very reasonable prediction of the onset of synchronization. This same approach also clearly shows that, as f_d/f_{St} is increased beyond unity, the number of P_N modes possible reduces, so that the complexity of the parameter space is greatest around $f_d/f_{St} = 1$.

Further, the amplitudes of oscillation at which the vortex shedding is completely suppressed have been predicted. This prediction matches reasonably well with the observation of the symmetric mode of vortex shedding, indicating that the symmetric mode occurs when the forcing completely suppresses the natural vortex shedding, allowing the flow to oscillate with the forcing only.

The definition of Γ_{1_2} as a function of f_d/f_{St} allows the prediction of the onset of the P_1 mode. Symmetry considerations show that this mode must be asymmetric, and that this mode can only occur for values of $f_d/f_{St} \leqslant 1$.

It is shown that practically all of the flow states encountered, from quasi-periodic to synchronized to symmetric, can be explained by the simple consideration of how the primary frequency of vortex shedding is modified by the oscillation.

Acknowledgements

The authors would like to acknowledge the financial support of the Australian Research Council (ARC) through grant number DP110102141 under the Discovery program. J.S.L. would like to acknowledge the financial support of the ARC through an Australian Postdoctoral Fellowship. The authors acknowledge Dr E. Konstantinidis for the contribution of the collated data shown in figure 18.

REFERENCES

AL-MDALLAL, Q. M., LAWRENCE, K. P. & KOCABIYIK, S. 2007 Forced streamwise oscillations of a circular cylinder: locked-on modes and resulting fluid forces. *J. Fluids Struct.* **23** (5), 681–701.

ARMSTRONG, B. J., BARNES, F. H. & GRANT, I. 1986 The effect of a perturbation on the flow over a bluff cylinder. *Phys. Fluids* **29**, 2095–2102.

ARNOL'D, V. I. 1965 Small denominators. I Mappings of the circumference onto itself. *Am. Math. Soc. Transl., Ser. 2* **46**, 215–284 (translated from 1961 *Izv. Akad. Nauk SSSR Ser. Mat.***25**, 1).

BARBI, C., FAVIER, D. P., MARESCA, C. A. & TELIONIS, D. P. 1986 Vortex shedding and lock-on of a circular cylinder in oscillatory flow. *J. Fluid Mech.* **170**, 527–544.

BARKLEY, D. & HENDERSON, R. D. 1996 Three-dimensional Floquet stability analysis of the wake of a circular cylinder. *J. Fluid Mech.* **322**, 215–241.

CETINER, O. & ROCKWELL, D. 2001 Streamwise oscillations of a cylinder in a steady current. Part 1. Locked-on states of vortex formation and loading. *J. Fluid Mech.* **427**, 1–28.

GRESHO, P. M. & SANI, R. L. 1987 On pressure boundary conditions for the incompressible Navier–Stokes equations. *Intl. J. Numer. Meth. Fluids* **7**, 1111–1145.

GRIFFIN, O. M. & RAMBERG, S. E. 1976 Vortex shedding from a cylinder vibrating in line with an incident uniform flow. *J. Fluid Mech.* **75** (2), 257–271.

HALL, M. S. & GRIFFIN, O. M. 1993 Vortex shedding and lock-on in a perturbed flow. *Trans. ASME: J. Fluids Engng* **115**, 283–291.

JARŻA, A. & PODOLSKI, M. 2004 Turbulence structure in the vortex formation region behind a circular cylinder in lock-on conditions. *Eur. J. Mech.* B/*Fluids* **23** (3), 535–550.

JAUVTIS, N. & WILLIAMSON, C. H. K. 2005 The effect of two degrees of freedom on vortex-induced vibration at low mass and damping. *J. Fluid Mech.* **509**, 23–62.

JEON, D. & GHARIB, M. 2004 On the relationship between the vortex formation process and cylinder wake vortex patterns. *J. Fluid Mech.* **519**, 161–181.

KARNIADAKIS, G. E. & SHERWIN, S. J. 2005 *Spectral/hp Element Methods for Computational Fluid Dynamics*. Oxford University Press.

KARNIADAKIS, G. E. & TRIANTAFYLLOU, G. S. 1989 Frequency selection and asymptotic states in laminar wakes. *J. Fluid Mech.* **199**, 441–469.

KIM, B. H. & WILLIAMS, D. R. 2006 Nonlinear coupling of fluctuating drag and lift on cylinders undergoing forced oscillations. *J. Fluid Mech.* **559**, 335–353.

KONSTANTINIDIS, E. & BALABANI, S. 2007 Symmetric vortex shedding in the near wake of a circular cylinder due to streamwise perturbations. *J. Fluids Struct.* **23**, 1047–1063.

KONSTANTINIDIS, E., BALABANI, S. & YIANNESKIS, M. 2003 The effect of flow perturbations on the near wake characteristics of a circular cylinder. *J. Fluids Struct.* **18**, 367–386.

KONSTANTINIDIS, E., BALABANI, S. & YIANNESKIS, M. 2005 The timing of vortex shedding in a cylinder wake imposed by periodic inflow perturbations. *J. Fluid Mech.* **543**, 45–55.

KONSTANTINIDIS, E., BALABANI, S. & YIANNESKIS, M. 2007 Bimodal vortex shedding in a perturbed cylinder wake. *Phys. Fluids* **19**, 011701.

KONSTANTINIDIS, E. & BOURIS, D. 2009 Effect of nonharmonic forcing on bluff-body vortex dynamics. *Phys. Rev.* E **79**, 045303(R).

KONSTANTINIDIS, E. & BOURIS, D. 2010 The effect of nonharmonic forcing on bluff-body aerodynamics at a low Reynolds number. *J. Wind Engng Ind. Aerodyn.* **98** (6–7), 245–252.

KONSTANTINIDIS, E. & LIANG, C. 2011 Dynamic response of a turbulent cylinder wake to sinusoidal inflow perturbations across the vortex lock-on range. *Phys. Fluids* **23**, 075102.

LE GAL, P., NADIM, A. & THOMPSON, M. C. 2001 Hysteresis in the forced Stuart–Landau equation: application to vortex shedding from an oscillating cylinder. *J. Fluids Struct.* **15**, 445–457.

LEONTINI, J. S., LO JACONO, D. & THOMPSON, M. C. 2011 A numerical study of an inline oscillating cylinder in a free stream. *J. Fluid Mech.* **688**, 551–568.

LEONTINI, J. S., STEWART, B. E., THOMPSON, M. C. & HOURIGAN, K. 2006 Wake state and energy transitions of an oscillating cylinder at low Reynolds number. *Phys. Fluids* **18** (6), 067101.

LEONTINI, J. S., THOMPSON, M. C. & HOURIGAN, K. 2007 Three-dimensional transition in the wake of a transversely oscillating cylinder. *J. Fluid Mech.* **577**, 79–104.

LO JACONO, D., LEONTINI, J. S., THOMPSON, M. C. & SHERIDAN, J. 2010 Modification of three-dimensional transition in the wake of a rotationally oscillating cylinder. *J. Fluid Mech.* **643**, 349–362.

MARZOUK, O. A. & NAYFEH, A. H. 2009 Reduction of the loads on a cylinder undergoing harmonic in-line motion. *Phys. Fluids* **21**, 083103.

MENEGHINI, J. R. & BEARMAN, P. W. 1995 Numerical simulation of high amplitude oscillatory flow about a circular cylinder. *J. Fluids Struct.* **9**, 435–455.

MUREITHI, N. W., HUYNH, K., RODRIGUEZ, M. & PHAM, A. 2010 A simple low order model of the forced Kármán wake. *Intl J. Mech. Sci.* **52**, 1522–1534.

MUREITHI, N. W. & RODRIGUEZ, M. 2005 Stability and bifurcation of a forced cylinder wake. In *Proceedings of 2005 ASME International Mechanical Engineering Congress and Exposition, Orlando, FL.*

NAZARINIA, M., LO JACONO, D., THOMPSON, M. C. & SHERIDAN, J. 2009 Flow behind a cylinder forced by a combination of oscillatory translational and rotational motions. *Phys. Fluids* **21** (5), 051701.

NISHIHARA, T., KANEKO, S. & WATANABE, T. 2005 Characteristics of fluid dynamic forces acting on a circular cylinder oscillated in the streamwise direction and its wake patterns. *J. Fluids Struct.* **20**, 505–518.

ONGOREN, A. & ROCKWELL, D. 1988 Flow structure from an oscillating cylinder. Part 2. Mode competition in the near wake. *J. Wind Engng Ind. Aerodyn.* **191**, 225–245.

PERDIKARIS, P. G., KAITSIS, L. & TRIANTAFYLLOU, G. S. 2009 Chaos in a cylinder wake due to forcing at the Strouhal frequency. *Phys. Fluids* **21**, 101705.

PROVANSAL, M., MATHIS, C. & BOYER, L. 1987 Bénard–von Kármán instability: transient and forced regimes. *J. Fluid Mech.* **182**, 1–22.

RODRIGUEZ, M. & MUREITHI, N. W. 2006 Cylinder wake dynamics in the presence of stream-wise harmonic forcing. In *Proceedings of PVP2006-ICPVT-11 2006 ASME Pressure Vessels and Piping Division Conference, Vancouver, BC, Canada*.

TANIDA, Y., OKAJIMA, A. & WATANABE, Y. 1973 Stability of a circular cylinder oscillating in uniform flow or in a wake. *J. Fluid Mech.* **61** (4), 769–784.

TATSUNO, M. 1972 Vortex streets behind a circular cylinder oscillating in the direction of flow. *Bull. Res. Inst. Appl. Mech. Kyushu Univ.* **36**, 25–37.

THOMPSON, M. C., HOURIGAN, K., CHEUNG, A. & LEWEKE, T. 2006 Hydrodynamics of a particle impact on a wall. *Appl. Math. Model.* **30**, 1356–1369.

THOMPSON, M. C., HOURIGAN, K. & SHERIDAN, J. 1996 Three-dimensional instabilities in the wake of a circular cylinder. *Exp. Therm. Fluid Sci.* **12**, 190–196.

TUDBALL-SMITH, D., LEONTINI, J. S., LO JACONO, D. & SHERIDAN, J. 2012 Streamwise forced oscillations of circular and square cylinders. *Phys. Fluids* **24**, 111703.

WILLIAMSON, C. H. K. 1988 The existence of two stages in the transition to three-dimensionality of a cylinder wake. *Phys. Fluids* **31** (11), 3165–3168.

WILLIAMSON, C. H. K. & ROSHKO, A. 1988 Vortex formation in the wake of an oscillating cylinder. *J. Fluids Struct.* **2**, 355–381.

XU, S. J., ZHOU, Y. & WANG, M. H. 2006 A symmetric binary-vortex street behind a longitudinally oscillating cylinder. *J. Fluid Mech.* **556**, 27–43.

YOKOI, Y. & KAMEMOTO, K. 1994 Vortex shedding from an oscillating circular cylinder in a uniform flow. *Exp. Therm. Fluid Sci.* **8**, 121–127.